


The profiles of bars in spiral galaxies

Peter Erwin ^{1,2}★ Victor P. Debattista ³ and Stuart Robert Anderson ³

¹Max-Planck-Institut für extraterrestrische Physik, Giessenbachstrasse, D-85748 Garching, Germany

²Universitäts-Sternwarte München, Scheinerstrasse 1, D-81679 München, Germany

³Jeremiah Horrocks Institute, University of Central Lancashire, Preston PR1 2HE, UK

Accepted 2023 June 27. Received 2023 June 26; in original form 2022 December 26

ABSTRACT

We present an analysis of major-axis surface-brightness profiles of bars in a volume-limited sample of 182 barred spiral galaxies, using *Spitzer* 3.6 μm images. Unlike most previous studies, we use the entire bar profile, and we classify profiles into four categories. These are ‘Peak+Shoulders’ (P+Sh) – updating the classic ‘flat bar’ profile – and three subtypes of the classic ‘exponential’ profile: (true) Exponential, ‘Two-Slope’ (shallow inner slope + steeper outer slope), and ‘Flat-Top’ (constant inner region, steep outer slope). P+Sh profiles are preferentially found in galaxies with high stellar masses, early Hubble types, red colours, and low gas fractions; the most significant factor is stellar mass, and previous correlations with Hubble type can be explained by the tendency of higher-mass galaxies to have earlier Hubble types. The most common type of non-P+Sh profile is Exponential, followed by Flat-Top profiles; all non-P+Sh profiles appear to have similar distributions of stellar mass, Hubble type, colour, and gas fraction. We also morphologically classify the bars of an inclined subsample into those with and without boxy/peanut-shaped (B/P) bulges; as previously reported, the presence of a B/P bulge is very strong function of stellar mass. Essentially all bars with B/P bulges have P+Sh profiles; we associate the profile shoulders with the outer, vertically thin part of the bar. We find a small number of P+Sh profiles in bars without clear B/P bulges, which may indicate that P+Sh formation precedes the formation of B/P bulges.

Key words: galaxies: bulges – galaxies: spiral – galaxies: structure.

1 INTRODUCTION

The majority of spiral galaxies with stellar masses of 10^9 – $10^{11} M_\odot$ have at least one stellar bar (e.g. Sheth et al. 2008; Díaz-García et al. 2016; Erwin 2018). Bars are found in both blue actively star-forming galaxies and in ‘red and dead’ systems, including S0 galaxies, and have been detected in galaxies with redshifts as high as ~ 2 (Guo et al. 2023). Given this prevalence, we might wonder if all bars are basically identical, or if they come in different forms, possibly linked to different host-galaxy characteristics, formation scenarios, or stages of development. One of the most fundamental and easily studied characteristics of bars – setting aside even more basic measurements like size – is their *radial surface-brightness profiles* (a manifestation of their stellar-density structure), which traditionally come in at least two varieties.

1.1 The traditional picture: Flat and exponential bar profiles

The classic pioneering study of bar profiles is that of Elmegreen & Elmegreen (1985), who studied surface-brightness profiles along the major and minor axes of bars in 15 barred spiral galaxies. They argued that bar profiles fell into two classes: ‘flat’ and ‘exponential’. The distinction was based on a comparison of the major-axis profile in the bar region to the same profile *outside* the bar (beyond the radius of the bar, in what they termed the ‘spiral’ region). Flat profiles tended

to have shallow or even constant surface-brightness profiles in the bar region, with the profile becoming steeper (and exponential) outside the bar. Exponential profiles, on the other hand, had bar profiles that were exponential, with slopes *at least as steep as* the profile outside the bar. They found evidence for a clear difference in Hubble types: flat profiles were preferentially found in earlier Hubble types, with exponential profiles in later types. Follow-up studies using near-IR imaging (Elmegreen et al. 1996; Regan & Elmegreen 1997) provided further support for this dichotomy.

It is important to bear in mind that what Elmegreen & Elmegreen (1985) meant by the term ‘flat’ is *not* that the profile must be literally flat (i.e. constant surface brightness as a function of radius), though it certainly does include such cases (as well as extreme cases where the profile gets brighter towards the end of the bar). They said, ‘each flat-bar galaxy has a surface brightness that decreases slowly or not at all with increasing distance along the bar, and decreases more rapidly along the spirals. We refer to these bar profiles as *flat* (i.e. flat when compared with the spiral profiles; some of these bar profiles are still ‘exponential-like,’ but their slopes are *smaller* than the slopes in the spiral regions).’

We emphasize this point because some subsequent studies have none the less interpreted the term literally, and then claimed that such profiles are less common. For example, Seigar & James (1998) analysed near-IR images of 40 barred galaxies and argued that there was no correlation with Hubble type, in contrast to the findings of Elmegreen & Elmegreen (1985). Inspection of their fig. 14 shows that what they call the ‘exponential’ profile of NGC 5737 is really of the flat type – though with less broad and dramatic shoulders than the

* E-mail: erwin@mpe.mpg.de

‘flat’ bars of IC 357 and IC 568 in the same figure.¹ Buta et al. (2006) analysed the *K*-band bar profiles of 26 S0–Sa galaxies and introduced an ‘intermediate’ class of profiles, in addition to flat and exponential. Inspection of their profiles shows this new class has the same basic ‘shallow+steep’ shape as in Elmegreen & Elmegreen (1985) – in fact, two of their ‘intermediate-profile’ galaxies (NGC 4596 and NGC 4608) were classified as flat by Elmegreen & Elmegreen.

More recent studies have focused on identifying flat versus exponential profile via 2D fits to galaxy images, using disc + bar + bulge models where the bar is a 2D elliptical structure with a Sérsic radial surface-brightness profile. In this approach, the ‘flatness’ of the bar profile is represented by the Sérsic index n , with lower values corresponding to flatter profiles.² Kim et al. (2015) modelled *Spitzer* IRAC1 (3.6 μ m) images of 144 low- and moderate-inclination barred galaxies from the *Spitzer* Survey of Stellar Structure in Galaxies (S⁴G; Sheth et al. 2010); they considered bar Sérsic indices $n < 0.4$ (i.e. sub-Gaussian) as representative of flat bars. Their main finding was that low- n bars were preferentially found in high-mass galaxies, with a transition mass of $\log(M_*/M_\odot) \sim 10.2$. They also argued that an even better separation could be had using the B/T value from their fits, with $B/T > 0.2$ having almost exclusively flat bars and ‘bulgeless’ ($B/T = 0$) galaxies having almost exclusively exponential-like bars. Kruk et al. (2018) performed 2D fits for 3461 barred galaxies using SDSS images and found a similar mass-based pattern: barred galaxies with $\log(M_*/M_\odot) \geq 10.25$ had a mean $n_{\text{bar}} = 0.43$, while lower-mass galaxies had a mean $n_{\text{bar}} = 0.81$ (nearly exponential). They too noted an association between prominent bulges and flatter bars, though this was based on the presence or absence of a bulge component in their best-fitting 2D models: ‘disc-dominated’ galaxies (where only a disc and bar components were needed in the model) had $n_{\text{bar}} = 0.92$, while ‘obvious bulge’ galaxies (where a bulge component was needed in addition to the disc and bar) had $n_{\text{bar}} = 0.40$. However, they did not find a correlation between B/T and n_{bar} within the ‘obvious bulge’ subsample itself.

Relatively little theoretical attention has been paid to the question of why a dichotomy in bar profiles might exist. Noguchi (1996) argued from N -body simulations that ‘spontaneous’ bars (formed via disc instabilities) had steep exponential profiles, while bars triggered by tidal interactions (in discs which were too hot to form bars spontaneously) had much flatter profiles, complete with ‘shoulders’ at the ends of the bar. However, Athanassoula & Misiriotis (2002) found that both types of bar profiles could be found in spontaneously formed bars. Combes & Elmegreen (1993) argued from their N -body simulations that flat-type profiles were associated with ‘early-type’ mass distributions (centrally concentrated large bulge/total mass ratios, often with an inner Lindblad resonance) and bars that extended to corotation, whereas bars in ‘late-type’ mass distributions retained the exponential profile of the disc. Very recently, Anderson et al. (2022) studied bar profiles in a number of N -body simulations, finding evidence that bar profiles transitioned from exponential-like to flat-type over time (and sometimes transitioned *back*) as part of the bars’ secular evolution (Beraldo e Silva et al. 2023 investigates the role of bar resonances in the evolution of these features).

We believe there are two reasons why now is a good time to revisit the question of bar profiles. The first is that past observational studies almost always involved relatively small heterogeneous samples,

making it difficult to draw firm conclusions about the prevalence of different profile types and their possible relation to other bar and galaxy parameters (partial exceptions to this trend are Kim et al. 2015 and Kruk et al. 2018, although they focused on fitting with simple 2D functions rather than detailed non-parametric analysis of profiles). There now exist sufficient high-S/N near-IR images with decent spatial resolution – in particular, as part of S⁴G – for larger unbiased samples of barred galaxies to be constructed.

Second, recent theoretical and observational studies have given us a much clearer understanding of what flat-bar profiles are really like, as we discuss in the following subsection.

1.2 New insights: The role of boxy/peanut-shaped bulges in bar profiles

A significant body of work (e.g. Combes et al. 1990; Raha et al. 1991; Kuijken & Merrifield 1995; Bureau & Freeman 1999; Athanassoula & Misiriotis 2002; Athanassoula 2005; Méndez-Abreu et al. 2008; Erwin & Debattista 2013; Wegg, Gerhard & Portail 2015; Blańa Díaz et al. 2017; Herrera-Endoqui et al. 2017) has demonstrated that many bars consist of two distinct, 3D stellar components: an outer region which is vertically thin and an inner region which is vertically thick, with a ‘boxy’ or ‘peanut-shaped’ appearance when seen from the side (i.e. in edge-on galaxies with the bar oriented close to perpendicular to the line of sight). This vertically thick inner part of the bar is thus usually referred to as the box/peanut or B/P bulge. When seen at intermediate inclinations, the B/P projects to form a broad, sometimes boxy, shape in the isophotes (the ‘box’ in the terminology of Erwin & Debattista 2013), while the outer vertically thin part of the bar appears as thin offset ‘spurs’ extending to larger radii. In systems close to face-on, the B/P bulge can still be identified as the rounder, inner part of the bar (a ‘barlens’, in the terminology of Laurikainen and collaborators). The studies of Erwin & Debattista (2017), Li, Ho & Barth (2017), Kruk et al. (2019), and Marchuk et al. (2022) found that such two-component bars are preferentially found in higher-mass galaxies, and thus in early-type spirals and S0s. This means that bars with B/P bulges appear to be found in the same types of galaxies that have flat-bar profiles.

This connection is important because modern investigations of B/P bulges in both real galaxies and simulations have shown that the B/P-bulge region has a distinct *steeper* surface-brightness profile compared to that of the outer part of the bar (Laurikainen et al. 2014; Athanassoula et al. 2015). This suggests that in bars with flat surface-brightness profiles, the inner part of the bar – interior to the classic flat part of the profile – should actually have a *steep* profile. Inspection of the profiles of classic flat-bar galaxies (e.g. Elmegreen & Elmegreen 1985; Elmegreen et al. 1996; Regan & Elmegreen 1997) shows that this is probably the case. In past studies, the inner parts of the bar profile were ignored, either because they were in a saturated part of the image or possibly because they were considered to belong to the ‘bulge’ and were thus not considered part of the bar.

Fig. 1 shows three examples of galaxies previously classified as having flat-bar profiles which have *also* been identified as having the morphological characteristics of B/P bulges. In all three cases, the region of the B/P bulge (spanned by the red arrows in the left-hand panels and bounded by vertical red lines in the right-hand panels) is associated with a much steeper surface-brightness profile, in contrast to the shallower profile outside, associated with the thinner and misaligned bar spurs.

¹ See Section 1.2 and Fig. 1 for definitions and examples of ‘shoulders’ in bar profiles.

² We remind the reader that the Sérsic profile is an exponential when $n = 1$ and a Gaussian when $n = 0.5$.

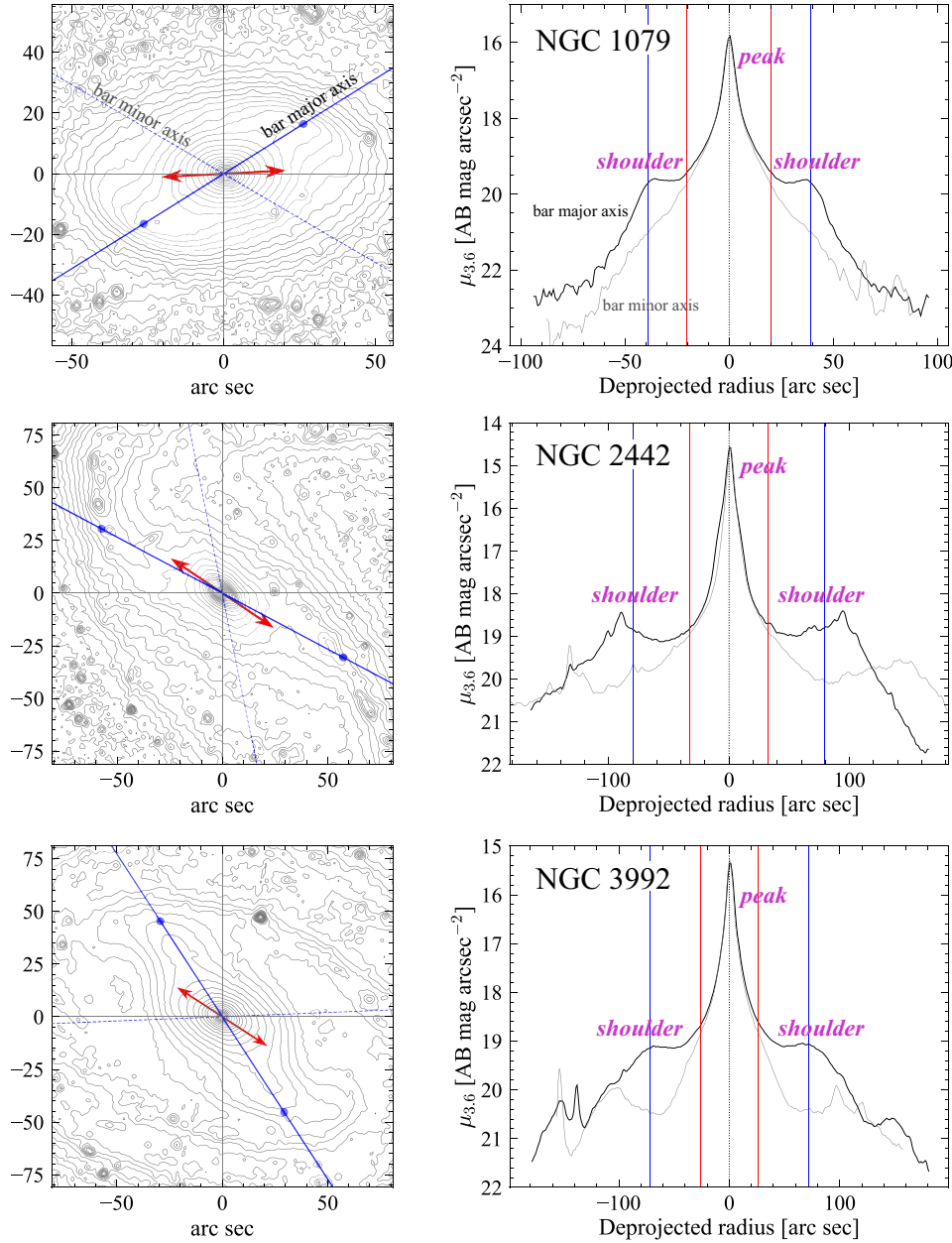


Figure 1. Plots of bar isophotes and profiles for three classic flat-bar galaxies, along with examples of the ‘peak’ and ‘shoulders’ sub-components: NGC 1079 (Buta et al. 2006), NGC 2442 (Elmegreen & Elmegreen 1985), and NGC 3992 (Regan & Elmegreen 1997). *Left:* Logarithmically spaced isophote contours from *Spitzer* 3.6 μ m images, showing the bar region. Thick diagonal blue lines indicate bar position angle, with blue dots marking approximate bar radius, while thinner dashed blue lines indicate the bar minor axis (as projected onto the sky); red arrows indicate position angle and approximate extent of B/P bulges in each galaxy (measurements from Erwin & Debattista 2013, 2017). *Right:* Profiles along bar major axis (thick black lines) and bar minor axis (thin grey lines), plotted against deprojected radius. Vertical red and blue lines mark B/P-bulge and bar radius, respectively; magenta labels indicate the approximate peak and shoulders sub-components of each profile. Note that the B/P-bulge radius delimits the steep inner peak of the profile, while the flatter shoulders extend to (and slightly beyond) the full bar radius.

Given our modern understanding of bars, then, we can argue that the classic flat-bar profile is better understood as a *two-part* profile. The inner region is steep and has usually been considered to be part of the (classical spheroidal) bulge (as has been done with recent 2D fitting of barred-galaxy images by, e.g. Kim et al. 2015 and Kruk et al. 2018), instead of actually being the inner part of the bar. The outer part is the ‘flat’ (or shallow) region, which is also marked, at the very end of the bar, by a break and a steep outer falloff that leads to the disc outside the bar. We suggest the term *shoulder* for the full

outer part of the profile: the interior shallower profile plus the break and falloff outside.³ We call the entire profile – the combination of

³This terminology is not original to us; earlier uses include, e.g. Noguchi (1996) for *N*-body bars and Gadotti et al. (2007) for real bars. This is also the same as what Athanassoula & Beaton (2006) termed a ‘hump’ in the profiles of M31’s bar and of some *N*-body bars.

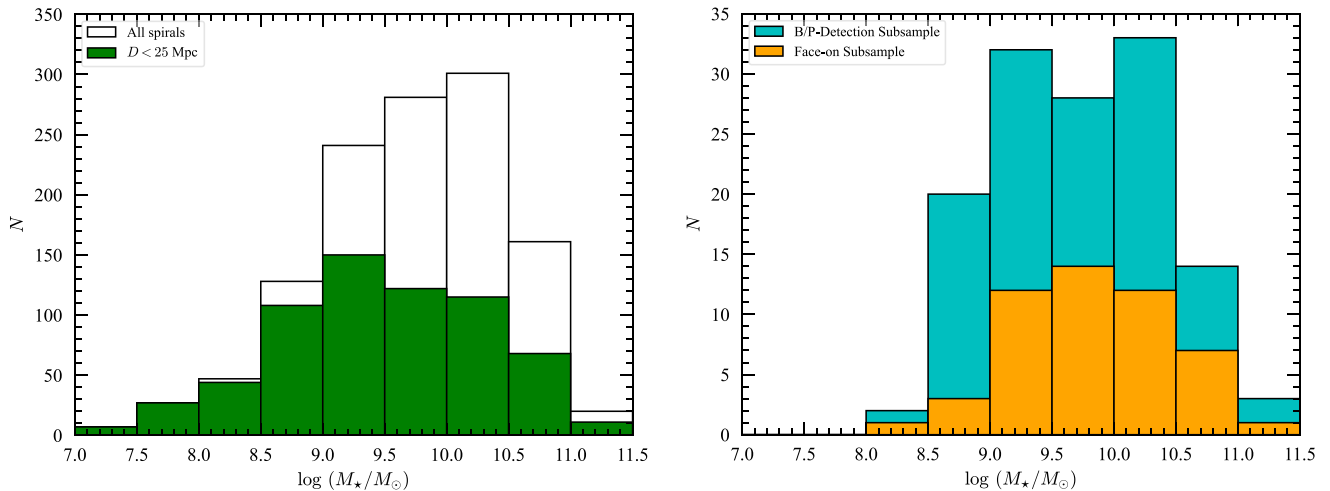


Figure 2. Left: Stellar-mass distributions for spiral galaxies in the parent spiral sample (hollow) and the $D < 25$ Mpc main spiral sample (green). Right: Same, but now for the two barred-galaxy subsamples [B/P-detection subsample (cyan) and Face-on subsample (orange)] analysed in this paper.

the shoulder with the steep inner part of the profile (with a central maximum) – **Peak+Shoulders**, or **P+Sh** for short.

1.3 Moving forward

If the traditional flat-bar profile is better understood as a two-part structure, could something similar be the case for exponential bar profiles? After all, these were also defined in Elmegreen & Elmegreen (1985) on the basis of only the outer parts of the bar (due to centrally saturated images), so it would be useful to know if they are truly, as the name implies, a single exponential profile that extends all the way in to the centre.

Our approach in this paper is to take a comprehensive look at local bar profiles using modern data and a relatively unbiased complete sample of galaxies. Specifically, we use near-IR imaging data from *Spitzer*, which minimizes possible confusion from dust and star formation,⁴ and we focus on the *entire* bar-major-axis profile, from the centre of the galaxy through the end of the bar. We do this for *all* bars in a volume- and mass-limited sample of spiral galaxies (not including lenticular galaxies). In the future, we also plan to compare our observational findings with the results of analysing bar profiles in barred galaxy simulations, as in Anderson et al. (2022).

Among the questions we hope to address are: Are all P+Sh profiles due to the presence of a B/P bulge? What do the central regions of exponential profiles look like? Can we identify any additional classes of bar profiles? Is there a more fundamental (physical?) driver of bar-profile type than Hubble type?

2 SAMPLE DEFINITIONS AND DATA SOURCES

2.1 Sample definitions

We started, following the general philosophy of Erwin (2018; 2019), with subsamples of the Díaz-García et al. (2016) subset of S⁴G: all disc galaxies in S⁴G with inclinations $i \leq 65^\circ$. We removed galaxies that lack distances and stellar masses in the compilation of Muñoz-Mateos et al. (2015), galaxies without reliable distances (i.e.

radial velocities of $< 500 \text{ km s}^{-1}$ and no non-redshift-based distance estimates), and galaxies with optical diameters below the formal S⁴G limit of $D_{25} = 1 \text{ arcmin}$. We also restricted the sample to spiral galaxies, due to the strong bias against S0 galaxies in S⁴G. This yielded the ‘parent spiral sample’, with 1220 galaxies.⁵ In the future, we plan to expand this analysis to include S0 galaxies.

We then applied a distance limit of 25 Mpc. This ensured good completeness down to a stellar mass of $\log(M_*/M_\odot) \sim 8.5$, as well as reasonable spatial resolution (median point spread function FWHM $\sim 165 \text{ pc}$), such that most bars can be successfully detected; see the discussion in Erwin (2018). This reduced the sample to 659 spirals (‘main spiral sample’), of which 370 have bars according to the catalogue of Herrera-Endoqui et al. (2015). The left-hand panel of Fig. 2 shows the stellar-mass distributions of the parent and main spiral samples.

We created two subsamples to analyse. The first – the **B/P-detection subsample** – was defined by selecting those galaxies with orientations best suited to allow us to determine if the bars did or did not have B/P bulges; the rationale was to allow us to test possible associations between B/P bulges (or the lack thereof) and bar profiles. Following the precepts of Erwin & Debattista (2017), we selected galaxies with inclinations $> 40^\circ$ and relative bar position angles $\Delta\text{PA}_{\text{dp}}$ (deprojected angle between bar and disc major axis) $< 60^\circ$. This yielded an initial set of 195 galaxies. We subsequently discarded 52 galaxies which proved, on closer inspection, to have dubious or non-existent bars (typically in low-mass late-type galaxies), along with five galaxies with erroneous inclinations (e.g. actually edge-on or face-on) and seven galaxies where bright stars close to or superimposed on the galaxies would interfere with the extraction of clean bar-major-axis profiles. (We also added one galaxy originally placed in the face-on subsample; see next paragraph.) This left us with a total of 132 galaxies in the B/P-detection subsample.

The second subsample – the **Face-on Subsample** – was meant to focus on *low-inclination* galaxies. We intended this as a comparison to the B/P-detection subsample, to see if differences in inclination might have any effects on our profile classifications. We selected

⁴We checked that hot dust and PAH from star formation does not significantly affect our profile classifications; see Section 2.2.

⁵This is the same as the ‘Parent Spiral Sample’ of Erwin (2018), but slightly different from the ‘Parent Spiral Sample’ of Erwin (2019).

galaxies from the main spiral sample with inclinations $\leq 30^\circ$, with no restrictions on bar orientation. After discarding six galaxies with dubious or non-existent bars and two galaxies actually too highly inclined,⁶ we were left with 50 galaxies in the face-on subsample. Taken together, our final combined subsamples comprise 182 galaxies.

The right-hand panel of Fig. 2 shows the stellar-mass distributions of both subsamples, which show no signs of being significantly different [Kolmogorov-Smirnov (K-S) test $P = 0.19$]. The strong decline for $\log(M_*/M_\odot) < 9$ is due in part to the low frequency of barred galaxies among low-mass galaxies (Erwin 2018).

2.2 Data sources

Our primary data source was the *Spitzer* IRAC1 (3.6 μm) images of the S⁴G sample. We used these for two purposes:

- (i) Extraction of the bar-major-axis and bar-minor-axis profiles;
- (ii) Identification of B/P-bulge morphologies.

Images were background-subtracted by taking the mean of several dozen median measurements in 20×20 -pixel boxes in relatively blank regions of the image well outside the galaxy. We note that accurate background subtraction is not essential for our purpose, since we are interested in the isophote shapes and surface-brightness profiles in the bright central regions of the galaxies.

Bar sizes and bar orientations were taken from Herrera-Endoqui et al. (2015); in 26 cases, we revised the bar position angles to better match the images. Bar strengths, when available, were taken from Díaz-García et al. (2016).⁷ Galaxy centre (pixel) coordinates, along with disc orientations (position angle of the major axis and inclination), were taken from Salo et al. (2015); we determined revised centres for 35 galaxies. For one galaxy (IC 796), we adopted a different disc position angle (144° , versus the 137° of Salo et al.) Stellar masses were taken from Muñoz-Mateos et al. (2015), while neutral gas masses were based on the m21c value in HyperLEDA, as described in Erwin (2018).⁸ Gas rotation velocities V_{rot} were taken from HyperLEDA, using their W_{gas} parameter corrected for inclination. Finally, global $g-r$ galaxy colours were based on the 2020 version of the Siena Galaxy Atlas (SGA-2020)⁹ – specifically, the total curve-of-growth g and r magnitudes (‘MTOT’). These are not available for 20 galaxies in the combined subsamples.

Detailed analysis of S⁴G images has suggested that when star formation is present, as much as ~ 10 – 30 per cent of the emission in the IRAC1 filter can be due to hot dust and polycyclic aromatic hydrocarbon (PAH) emission rather than old stars (Meidt et al. 2012; Querejeta et al. 2015). To check how much this might contaminate our profiles, we downloaded ‘stellar’ images from IRSA (as produced by ‘Pipeline 5’ in Querejeta et al. 2015) for a subset of our samples and generated bar-major-axis profiles from them to compare with the profiles from the original IRAC1 images. (Only ~ 55 per cent of our galaxies have stellar images from Pipeline 5.) Although there are localized differences, the

overall forms of the profiles do not change meaningfully between the IRAC1 and stellar images, and thus our classifications do not change.

3 CLASSIFICATION OF BAR PROFILES

3.1 The four types of bar profiles

Our starting point for bar-profile classifications was the original Elmegreen & Elmegreen (1985) ‘flat’ and ‘exponential’ classes. As discussed in Section 1, we recognize that ‘flat’ profiles are only shallow or flat in their outer parts; in most if not all cases, these bars have steep inner profiles, which appear to be at least partly due to the inner B/P structure of the bar. Because of this, we departed from Elmegreen & Elmegreen (1985) and most subsequent work by considering the *entire* profile, from the centre of the galaxy ($r = 0$) out to the end of the bar, even though this will inevitably include some contribution in the central part of the profile from non-bar components such as classical bulges, nuclear discs, nuclear star clusters, etc. Consequently, we began by replacing the term ‘flat’ with the term **Peak+Shoulders (P+Sh)**; this reflects both the full outer part of the bar profile (the shoulder) and the steep inner component (the peak).

Given this approach, we also considered the entire profile ($r \geq 0$) of ‘exponential’ bars. Exploratory analysis of bar-major-axis profiles from our sample suggested that when this is done, there is actually more than one type of ‘exponential’ profile. That is, among the profiles which were *not* P+Sh, we found many with genuinely single-exponential profiles, but also a number with more complicated forms. We eventually settled on a total of *three* classes of non-P+Sh bar profiles. Figs (3)–(5) show examples of these three types of bar profiles. Note that some of these profiles do show compact central peaks, plausibly consistent with nuclear star clusters; we note the existence of such features, but otherwise ignore them in our analysis.

In summary, we found evidence for *four* general classes of bar profile:

- (i) **Peak+Shoulders (P+Sh)** – This is our updated version of the classic ‘flat’ profile of Elmegreen & Elmegreen (1985); it includes the ‘intermediate’ class of Buta et al. (2006). See Fig. 1 for examples.
- (ii) **Exponential (Exp)** – These are profiles which approximate a single exponential over their whole range, with the possible addition of a small central excess compatible with a very compact bulge or a nuclear star cluster. See Fig. 3 for examples.
- (iii) **Two-Slope (2S)** – These are profiles where the inner part is a shallow exponential, breaking beyond a certain radius (either inside the bar or sometimes at the bar end) to a steeper exponential. See Fig. 4 for examples.
- (iv) **Flat-Top (FT)** – This can be thought of as an extreme version of the previous profile: the inner part has essentially constant surface brightness, breaking to an exponential profile beyond a certain radius. This is distinguished from the P+Sh profile by the fact that it has no central ‘peak’.¹⁰ See Fig. 5 for examples.

⁶One galaxy had an inclination of $\sim 32^\circ$; the other had both inclination and bar orientation appropriate for the B/P-detection subsample, so we added it to the latter.

⁷Of the 182 galaxies in our combined subsamples, 147 have deprojected ellipticity values, 142 have $A_{2,\text{max}}$ values, and 105 have $A_{4,\text{max}}$ values.

⁸For NGC 4314, which has no m21c value in HyperLEDA, we use the H I flux in Springob et al. (2005).

⁹<https://www.legacysurvey.org/sga/sga2020/>

¹⁰That is, these are profiles with shoulders, but no ‘heads’ – headless or decapitated profiles. (We considered referring to these as ‘Green Knight’ profiles, but decided against such an obscure literary reference.)

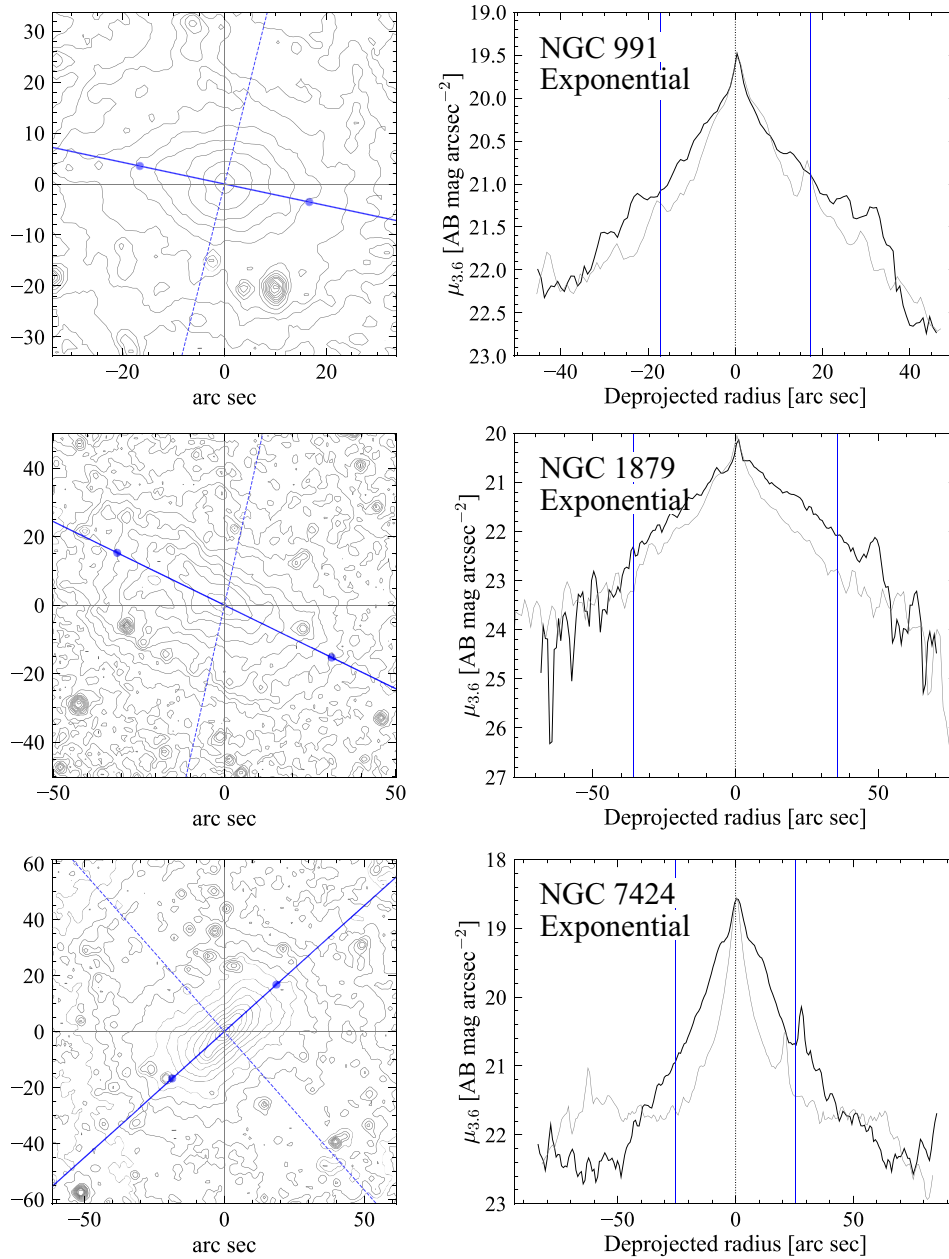


Figure 3. As for Fig. 1, but showing examples of galaxies with exponential (Exp) bar profiles. Left: *Spitzer* 3.6 μm isophotes. Thick (solid) and thin (dashed) blue lines indicate bar major-axis and minor-axis position angles, respectively (as projected onto the sky); blue circles mark the approximate radius of the bar. Right: Profiles along bar major axis (solid lines) and minor axis (thin grey lines). Vertical blue lines indicate bar radius.

3.2 How we did the classifications

Having defined a preliminary classification scheme (see previous section), we then performed a general visual classification of all 182 bar-major-axis profiles in the two subsamples. To minimize the possibility of biased classifications, we used a blinded approach where profile plots were automatically generated and assigned numbers from a randomized ordering. These profiles were then classified by two of the authors (PE and VPD). By randomizing the profiles and obscuring their origins, we hoped to avoid possible biases that might result from knowing the individual-galaxy origins of profiles (e.g. recognizing a galaxy name as that of a classic well-studied ‘flat’ or ‘exponential’ profile from the literature), knowledge

of whether a profile was from a galaxy with an identified B/P bulge, knowledge of a galaxy’s likely stellar mass,¹¹ etc. See Appendix A for examples of the actual plots used for the blind classification process.

The agreement between the two classifiers was reasonably good, with disagreements on 24 of the 182 galaxies. The majority of these disagreements involved exponential sub-types (e.g. exponential versus flat-top); only eight involved one classifier choosing P+Sh and the other choosing one of the exponential sub-types. In general, we

¹¹In practice, there is the possibility that one could guess that a very noisy profile came from a low-mass, low-surface-brightness galaxy.

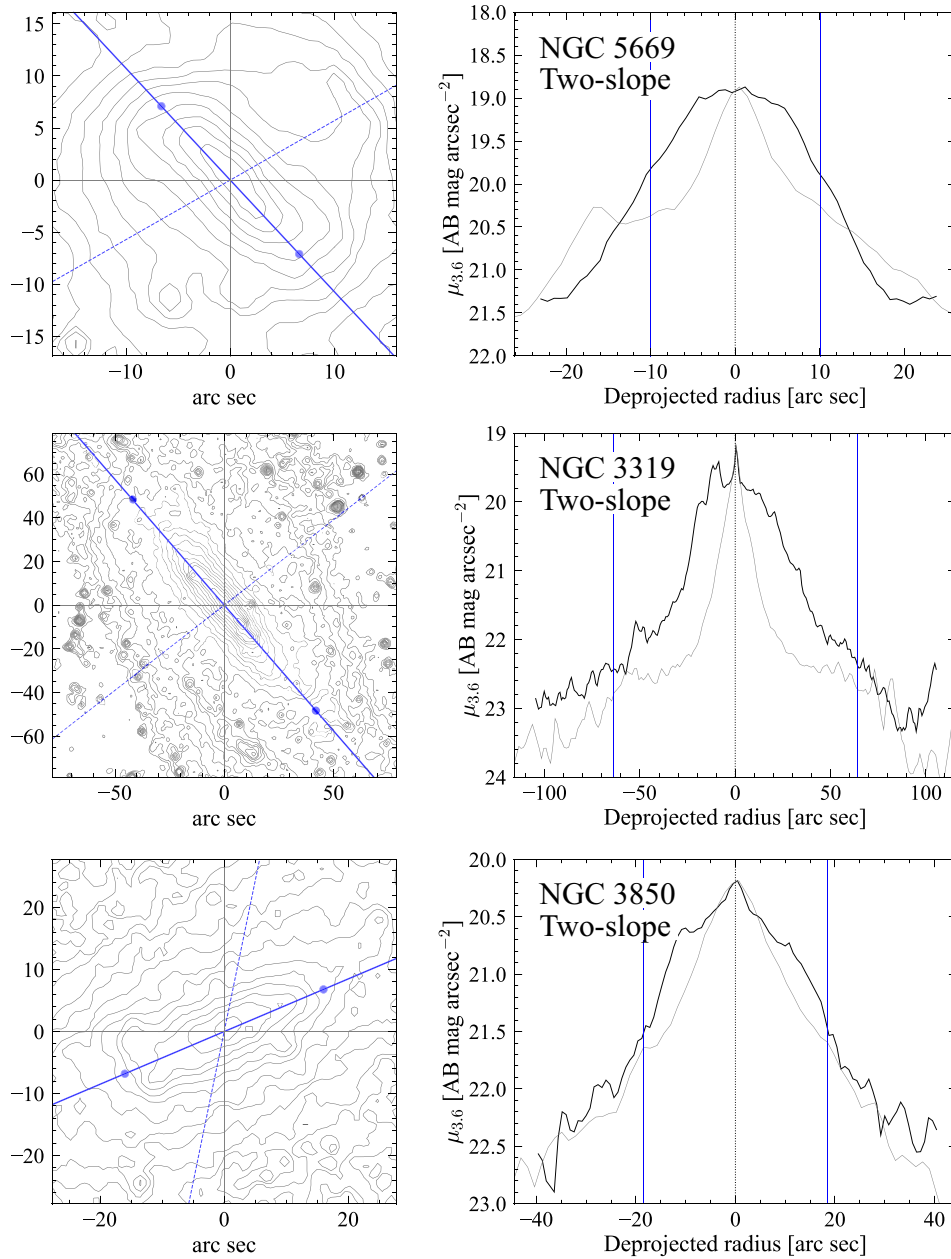


Figure 4. As for Fig. 3 but now showing examples of galaxies with two-slope (2S) bar profiles. Note that NGC 3319 has a small nuclear peak, consistent with a nuclear star cluster (e.g. Georgiev & Böker 2014); NGC 3850 may have a weaker example.

count profile types only for galaxies where both classifiers agreed, though for overall fractions of profile types we also report results based on giving each vote for classification X a value of 1 and then dividing the totals by two. Thus, a disagreement counts as 1/2 a vote for each of the two profile types.

4 RESULTS FOR PROFILE CLASSIFICATIONS

4.1 General results

The two most common profile types we find in our galaxies are P+Sh (31^{+4}_{-3} percent of the combined subsamples) and exponential (41 ± 4 percent); flat-top profiles are the next most common (12^{+3}_{-2} percent), with only a small number of bars showing two-

slope profiles ($3.3^{+1.6}_{-1.1}$ percent), along with 12^{+3}_{-2} percent split classifications.¹² What is potentially more interesting than these raw percentages is whether the profiles type depends on particular galaxy characteristics.

We show the distribution of bar-profiles types as a function of stellar mass in Fig. 6. Results from the two different classifiers appear in the left and right columns, respectively; these show very good agreement. The top row has classifications for all galaxies in both subsamples, while the middle and bottom rows show the classifications for the B/P-detection and face-on

¹²If we count split classifications as 1/2 for each, then the frequencies are 33^{+4}_{-3} percent for P+Sh, 45 ± 4 percent for Exponential, 17 ± 3 percent for Flat-Top, and $4.7^{+1.8}_{-1.4}$ percent for Two-Slope.

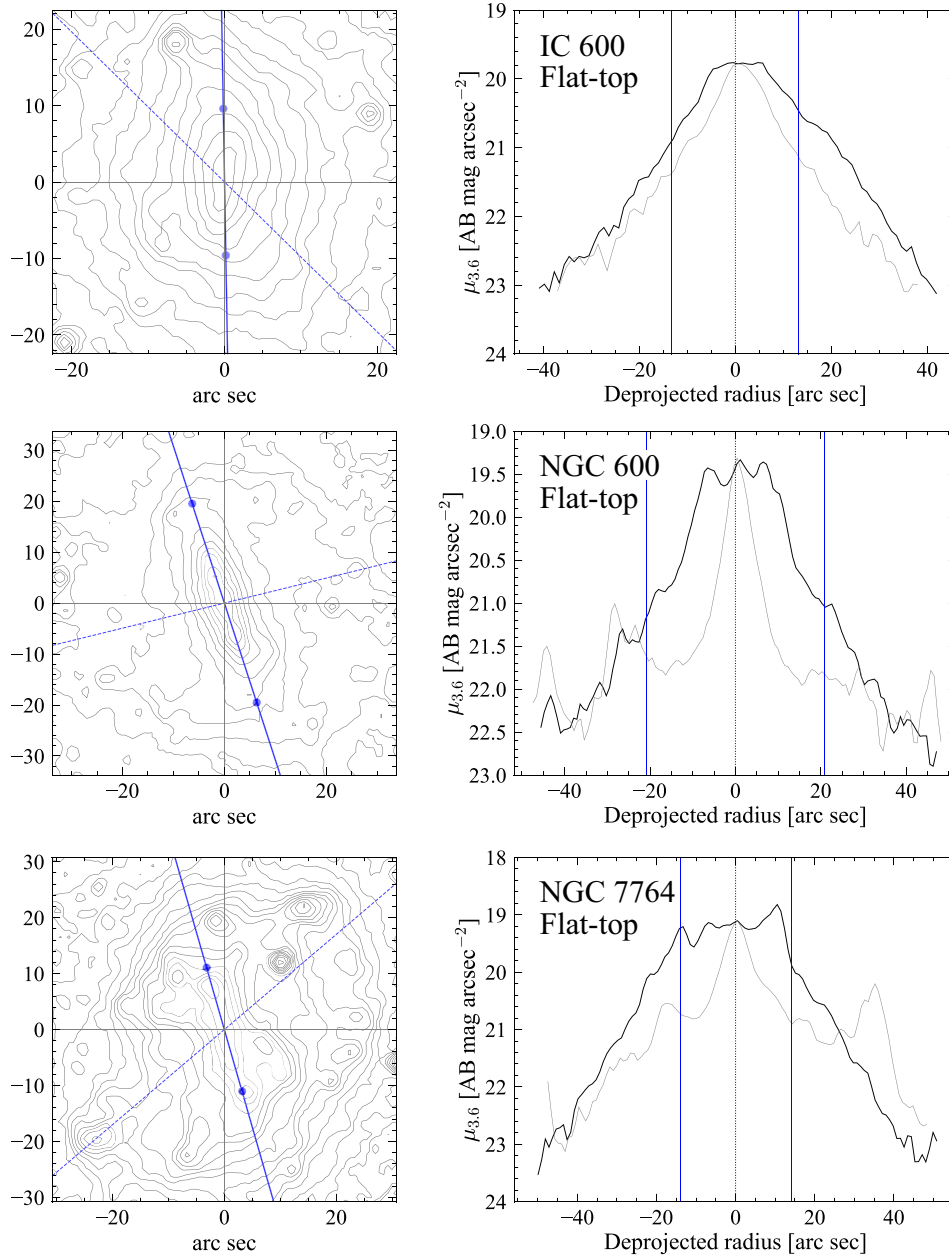


Figure 5. As for Fig. 3 but now showing examples of galaxies with flat-top (FT) bar profiles.

subsample, respectively. We see no significant differences for the two subsamples (K-S $P = 0.50$ – 0.88), which suggests that inclination does not meaningfully affect the appearance of the bar profiles.

The clearest trend is the mass segregation between the P+Sh bars and the others. P+Sh bars are preferentially found in high-mass galaxies, especially $\log(M_*/M_\odot) \gtrsim 10$. The other profile types, which are dominated by exponential bars, are preferentially found in lower-mass galaxies, and seem to share the same basic distribution in stellar mass. A K-S test comparing the stellar mass distributions of exponential and flat-top profiles yields $P = 0.77$ for the PE classifications and 0.39 for the VPD classifications, so there is no evidence for a difference in their parent samples.

Fig. 7 shows the distributions of Hubble types (top), neutral gas mass fraction (middle), and $g-r$ colour for each profile type, with classifications from both PE and VPD merged. As was originally

pointed out by Elmegreen & Elmegreen (1985), P+Sh profiles (their ‘flat’ profiles) are typically found in earlier Hubble types, while the exponential and other profiles become common only for Sc and later galaxies. We can also see that gas-poor galaxies are more likely to have P+Sh profiles, while gas-rich galaxies tend to have a mix of the non-P+Sh profiles. A similar trend holds for colour, with red galaxies more likely to have P+Sh profiles. This is consistent with the stellar-mass and Hubble-type trends, in that high-mass galaxies (and earlier Hubble types) tend to be redder and more gas-poor than low-mass galaxies (and later Hubble types). We examine the question of whether there is an *independent* relation between profile type and any of these three parameters in Section 4.2.

Finally, in Fig. 8 we show distributions of *bar* characteristics for the different profile types. The upper left-hand panel shows relative bar size (bar radius divided by the exponential-disc scale length from the 2D fits of Salo et al. 2015), while the other panels

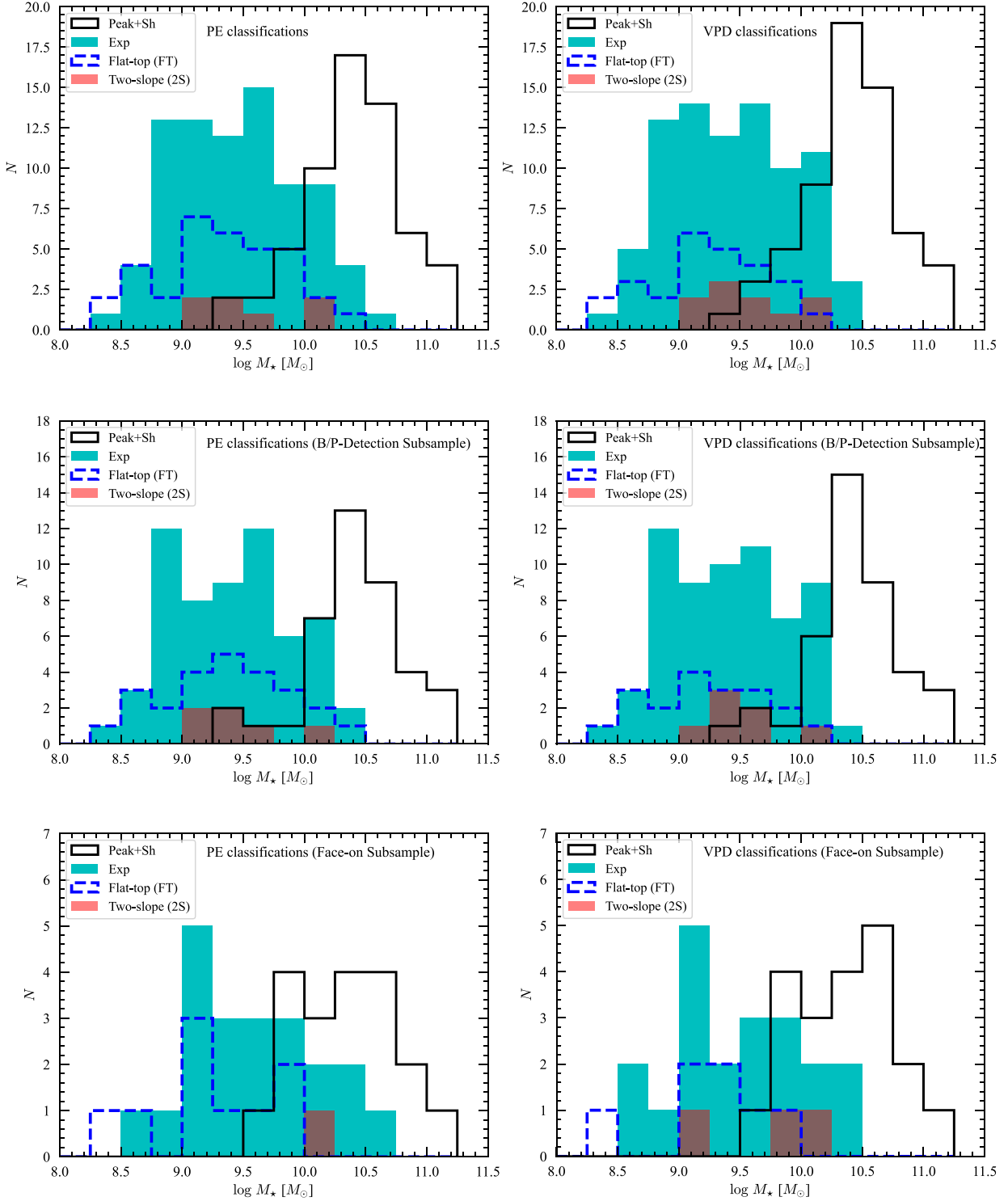


Figure 6. Distribution of bar-profile classifications as a function of galaxy stellar mass, as determined by the two classifiers. Top row: classifications for all spiral galaxies. Middle row: Classifications for galaxies with moderate inclinations and low ΔPA_{dp} . Bottom row: Classifications for galaxies with near-face-on orientations.

show three different measurements of bar ‘strength’, all taken from Díaz-García et al. (2016): deprojected maximum isophotal ellipticity of the bar, maximum $m = 2$ Fourier amplitude relative to the $m = 0$ amplitude $A_{2,max}$, and maximum relative $m = 4$ amplitude $A_{4,max}$.

For bar sizes, we see only a weak difference between P+Sh and non-P+Sh profiles, though it is formally statistically significant (K-S $P \sim 0.0006$, versus $P \sim 3 \times 10^{-14}$ for $\log f_{gas}$ and $P \sim 1 \times 10^{-18}$ for Hubble type). The fact that P+Sh bars tend to be relatively larger is plausibly explained by the strong stellar-mass dependence,

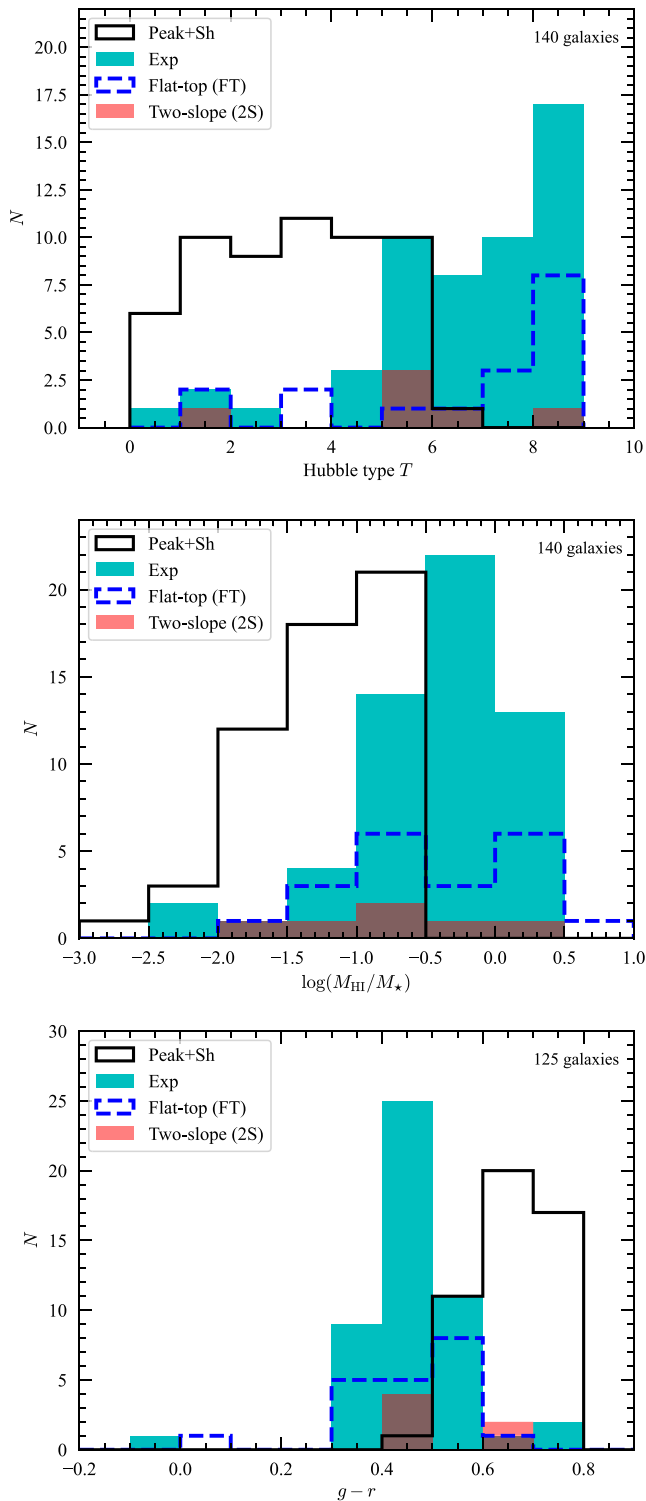


Figure 7. Distribution of bar-profile classifications as a function of galaxy Hubble type T (top), H I mass fraction (middle), and $g-r$ colour (bottom), as determined by the two classifiers for all spiral galaxies. In contrast to Fig. 6, here we show distributions for galaxies where both classifiers agree on the profile type, combining both subsamples. The number of galaxies are indicated in the upper-right corners of each plot (some galaxies do not have $g-r$ colours).

since relative bar sizes tend to be larger for galaxies with masses $\log(M_*/M_\odot) > 10.2$ (Erwin 2019).

When we turn to bar ellipticity, there is a slight tendency for P+Sh profiles to appear in stronger bars. However, there is considerable overlap, so that (for example) bars with a deprojected ellipticity of 0.4 are equally likely to have P+Sh profiles or exponential profiles. In fact, when the different non-P+Sh profiles are combined, their deprojected ellipticity distributions basically reproduce that of the P+Sh galaxies (K-S test $P = 0.95$). There is, in contrast, some evidence for a difference between the exponential profiles and the combination of 2S and FT profiles, in that the latter tend to be found in more elliptical bars (K-S test $P = 0.0005$).

For $A_{2,\max}$ and $A_{4,\max}$, P+Sh profiles appear somewhat biased toward stronger bars (higher values of $A_{2,\max}$ and $A_{4,\max}$; K-S $P = 0.0011$ and 0.035 , respectively). The lower significance for the $A_{4,\max}$ comparison might simply reflect the lower number of galaxies with $A_{4,\max}$ measurements. Again, however, there is considerable overlap, and the segregation of profile types is nowhere near as strong as it is for stellar mass (or, indeed, for Hubble type, gas fraction, or colour).

In summary, we find that bar-profile type is very strongly dependent on galaxy stellar mass, in the sense that P+Sh profiles are overwhelmingly found in massive galaxies, while the various exponential sub-types (Exp, FT, 2S) are found in low-mass galaxies. Similar trends are found for Hubble type, gas mass fraction, and $g-r$ colour, with P+Sh profiles preferentially found in galaxies with earlier Hubble types, lower gas fractions, and redder colours. On the other hand there is only weak or ambiguous evidence that bar-profile class depends on relative bar size or bar strength.

In the next section, we focus on the question of whether the observed strong trends with stellar mass, Hubble type, gas fraction, and colour are independent, or whether profile type might depend mostly or entirely on just one of these characteristics, with the other trends being side effects of known correlations between all four parameters.

4.2 Dependence of bar-profile type on single versus multiple parameters

We have seen that P+Sh profiles are more common in galaxies with higher stellar masses, lower gas mass fractions, redder colours, and earlier Hubble types. The question that naturally arises is whether these trends are *independent*, because galaxy mass is correlated with colour and inversely correlated with gas fraction and Hubble type. Is the dependence on these other characteristics merely a side effect of a more general trend with stellar mass? If we could, for example, compare barred spirals with the same stellar mass, would P+Sh profiles still be more common in galaxies with lower gas fractions, redder colours, or earlier Hubble types?

We attempt to answer these questions via logistic regression, which models the probability of a galaxy having a given binomial characteristic as a function of one or more parameters. This is appropriate for our problem because the visible trends show clear segregation by parameter value: e.g. all galaxies with $\log(M_*/M_\odot) \lesssim 9.2$ do not have P+Sh profiles, while all galaxies with $\log(M_*/M_\odot) \gtrsim 10.6$ do, with the P+Sh fraction increasing more or less monotonically with increasing stellar mass (see Fig. 11). Specifically, we focus on the presence or absence of a P+Sh profile, counting only cases where both classifiers agreed on its presence; galaxies with split classifications are counted as non-P+Sh.

Logistic regression involves modelling the probability P of a galaxy having a particular characteristic – e.g. a P+Sh profile – as a function of one or more parameters and one or more independent

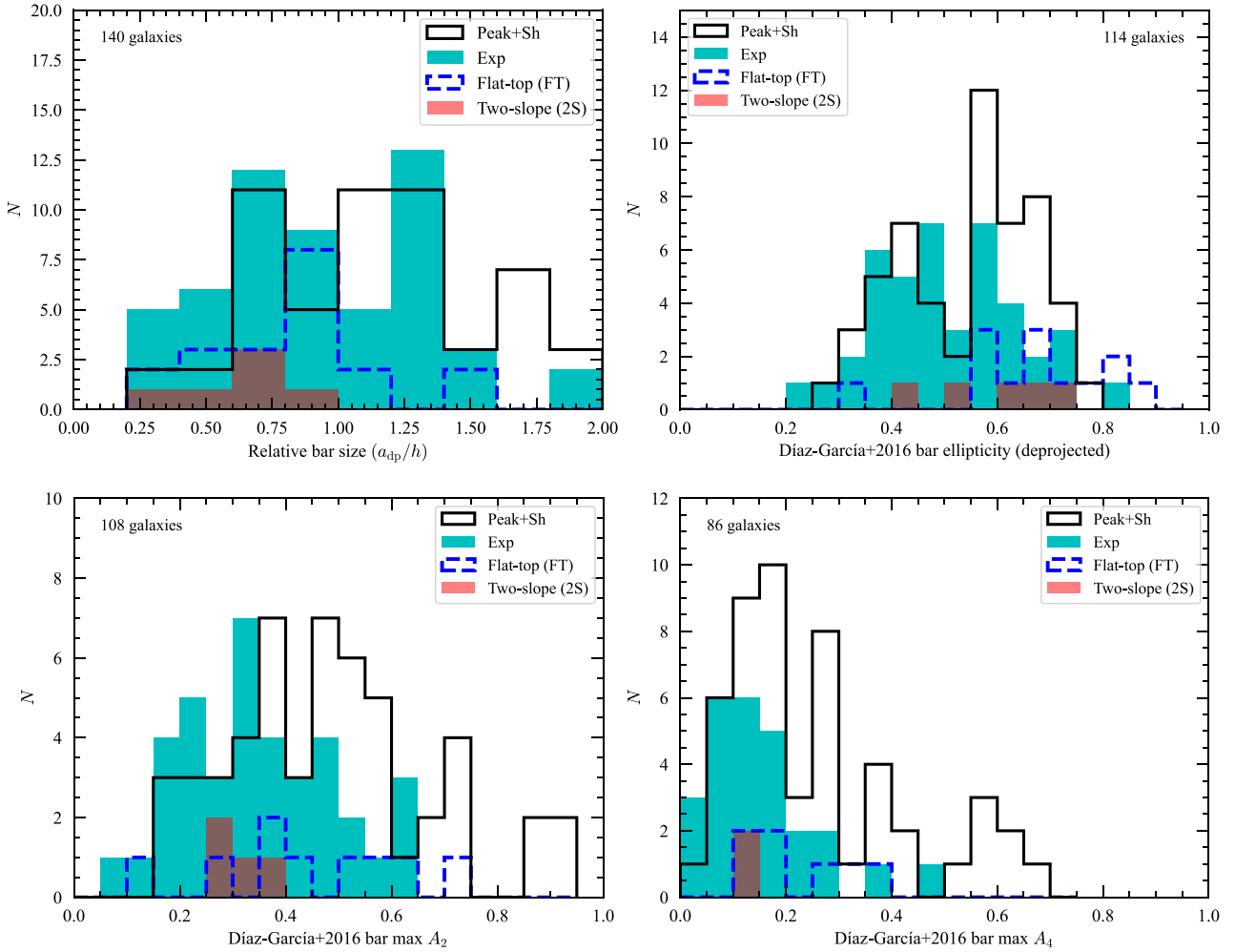


Figure 8. As for Fig. 7, but now showing distribution of bar-profile classifications as a function of relative bar size (deprojected semi-major axis divided by exponential disc scale length, upper left) and three different measurements of bar strength: deprojected isophotal ellipticity and maximum $m = 2$ and $m = 4$ Fourier amplitudes (relative to $m = 0$ amplitudes). The total number of galaxies with valid measurements is indicated in the upper corners of each plot.

variables via the logistic equation

$$P = \frac{1}{1 + e^{-(\alpha + \sum_i \beta_i x_i)}}, \quad (1)$$

where the x_i are the different variables (e.g. stellar mass, gas fraction, and Hubble type); the probability asymptotes to 0 as $x_i \rightarrow -\infty$ and to 1 as $x_i \rightarrow +\infty$ (for $\beta_i > 0$, with the reverse behaviour for $\beta_i < 0$). If a given parameter x_i has no relation to the P+Sh probability, then we would expect the corresponding slope β_i to be ≈ 0 .

The best-fitting values of the parameters can be determined using a maximum likelihood approach,¹³ with the total likelihood being the product of the individual Bernoulli likelihoods for each of the N observed galaxies

$$\mathcal{L} = \prod_{n=1}^N P_n^{y_n} (1 - P_n)^{1-y_n}, \quad (2)$$

where P_n is the probability for galaxy n (evaluated using equation 1) and y_n is the observed result ($=1$ if the galaxy has that characteristic and 0 if it does not).

¹³We use the standard `glm` function in the R statistical language.

We can investigate the relative importance of different parameters by performing individual fits using just one parameter and then comparing the relative goodness of each fit. We can also fit using multiple parameters simultaneously and look at the relative significance of the different parameters in such fits.

4.2.1 Dependence on single parameters

Table 1 compares single-variable logistic fits for individual galaxy parameters. For each of several subsamples,¹⁴ we show the best-fitting intercept α and slope β , along with the associated probability $P_{\beta=0}$ for a slope at least that different from zero under the null hypothesis that the true slope is zero.

We also show the AIC value for the fits, as computed by the R function `glm`:

$$\text{AIC} = -2 \ln \mathcal{L} + 2k, \quad (3)$$

¹⁴Note that unlike the subsample counts in Figs 7 and 8, which used only galaxies where both classifiers agreed on the final classification, these subsamples included galaxies where both classifiers agreed on whether a galaxy was P+Sh or not, but may have disagreed on the non-P+Sh class.

Table 1. Logistic regression for P+Sh Profiles: Single variables.

Variable (1)	α (2)	β (3)	$P_{\beta=0}$ (4)	AIC (5)
Full sample (182 galaxies)				
$\log M_*$	-47.71	4.70	1.0×10^{-10}	112.72
Hubble type T	2.95	-0.76	1.0×10^{-11}	140.98
$\log f_{\text{gas}}$	-2.84	-2.48	6.7×10^{-10}	164.67
B/P-detection subsample (132 galaxies)				
$\log V_{\text{rot}}$	-34.50	16.24	6.7×10^{-8}	78.23
$\log M_*$	-50.80	4.99	1.3×10^{-7}	74.79
Hubble type T	2.71	-0.70	1.4×10^{-8}	106.95
$\log f_{\text{gas}}$	-2.65	-2.23	4.8×10^{-7}	122.65
Full sample: galaxies with $g-r$ and $A_{2,\text{max}}$ (125 galaxies)				
$\log M_*$	-44.25	4.37	2.3×10^{-8}	91.23
$g-r$	-13.19	22.40	5.0×10^{-9}	88.13
$A_{2,\text{max}}$	-2.17	4.02	0.00021	154.00
Hubble type T	3.61	-0.87	2.1×10^{-8}	102.97
$\log f_{\text{gas}}$	-2.70	-2.68	2.8×10^{-7}	123.27
B/P-detection subsample: galaxies with $g-r$ (118 galaxies)				
$\log V_{\text{rot}}$	-32.58	15.33	2.4×10^{-7}	70.42
$\log M_*$	-48.38	4.75	4.7×10^{-7}	67.69
$g-r$	-12.13	19.67	1.8×10^{-8}	75.43
Hubble type T	2.96	-0.76	6.4×10^{-8}	91.07
$\log f_{\text{gas}}$	-2.81	-2.50	1.2×10^{-6}	105.80

Notes. Results of single-variable logistic regressions: probability of a barred spiral having a Peak+Shoulders profile as function of values of different parameters. Each line represents a separate logistic regression. (1) Galaxy parameter used in fit (M_* = stellar mass; f_{gas} = gas mass ratio; V_{rot} = inclination-corrected gas rotation velocity). (2) Intercept value for fit. (3) Slope for fit. (4) P -value for slope. (5) Akaike information criterion (AIC) value for fit; lower values indicate better fits for a given sample.

where \mathcal{L} is the (maximized) likelihood value (equation 2) and k is the number of (free) parameters. Smaller values of AIC indicate a better fit for a given data set. Traditionally, values of $|\Delta\text{AIC}| < 2$ are considered non-significant, while $|\Delta\text{AIC}| \approx 2-6$ is weak evidence in favour of the model with lower AIC and $|\Delta\text{AIC}| > 6$ is considered strong evidence. We note that the latter criterion corresponds to $P < 0.05$, and so is not ‘strong evidence’ by the usual standards of astronomy; $|\Delta\text{AIC}| \gtrsim 12$ would be a rough equivalent to a 3σ standard of significance.

This allows us to see which individual parameters are *most important*. What is clear is that the key parameters are those related to galaxy mass, and possibly colour. For most of the samples, it is the galaxy stellar mass that provides the best fit, although $\log V_{\text{rot}}$ is only marginally worse. For the subset of the full sample with colour data, it is $g-r$ (but note that this is not true for the B/P-detection subsample), though with $|\Delta\text{AIC}|$ only ≈ 4 .

While the fits using other parameters ($\log f_{\text{gas}}$, $A_{2,\text{max}}$, Hubble type) are all formally significant (i.e. they have small values of $P_{\beta=0}$), they are clearly worse than galaxy mass or $g-r$ as predictors (they have much larger values of AIC), and it is possible that these are merely side-effects of correlations between, e.g. galaxy mass and the other parameters. The question then becomes: do any of the non-mass parameters have any *independent* effect on the presence of P+Sh profiles?

4.2.2 Dependence on multiple parameters

Table 2 is similar to Table 1, except that it shows one or two *multiparameter* logistic fits for each subsample. Here, we look at two things: which of the parameters in each fit have slopes that

Table 2. Logistic regression for P+Sh profiles: Multiple variables.

Variable (1)	α (2)	β (3)	$P_{\beta=0}$ (4)	AIC (5)
Full sample (182 galaxies)				
$\log M_*$	-36.62	3.80	1.3×10^{-6}	102.99
Hubble type T		-0.48	0.01	
$\log f_{\text{gas}}$		0.02	0.98	
B/P-detection subsample (132 galaxies)				
$\log M_*$	-42.06	4.32	1.4×10^{-5}	73.90
Hubble type T		-0.39	0.074	
$\log f_{\text{gas}}$		0.27	0.73	
$\log V_{\text{rot}}$	-24.97	12.61	4.3×10^{-5}	75.19
Hubble type T		-0.42	0.072	
$\log f_{\text{gas}}$		-0.04	0.96	
Full sample: galaxies with $g-r$ and $A_{2,\text{max}}$ (125 galaxies)				
$\log M_*$	-33.96	2.83	0.0031	78.99
$g-r$		11.72	0.035	
$A_{2,\text{max}}$		1.51	0.36	
Hubble type T		-0.35	0.18	
$\log f_{\text{gas}}$		0.72	0.37	

Notes. As for Table 1, but now showing results of multiple-variable logistic regressions: probability of a barred spiral having a Peak+Shoulders profile as function of values of three or more different parameters at the same time. For the B/P-detection subsample, we performed two fits, using either $\log(M_*/M_\odot)$ or $\log V_{\text{rot}}$ as a ‘galaxy mass’ variable. The lines show the best-fitting coefficients for the specified variables; the first line also includes the intercept (α) and the AIC value for the fit. (1) Galaxy parameters used in fit. (2) Intercept value for fit. (3) Slope for each parameter in fit. (4) P -value for slope. (5) AIC value for fit.

Table 3. Logistic regression for presence of B/P bulges.

Variable (1)	α (2)	β (3)	$P_{\beta=0}$ (4)	AIC (5)
$\log M_*$	-63.62	6.18	3.7×10^{-6}	61.85
$\log V_{\text{rot}}$	-58.51	27.26	1.2×10^{-5}	48.12

Note. Results of single-variable logistic regressions: probability of a barred spiral having a B/P bulge as function of stellar mass or rotation velocity for the B/P-detection subsample. (1) Galaxy parameter used in fit (M_* = stellar mass; V_{rot} = gas rotation velocity). (2) Intercept value for fit. (3) Slope for fit. (4) P -value for slope. (5) AIC value for fit.

differ from zero in a statistically significantly sense (small values of $P_{\beta=0}$), and which fits have AIC values significantly smaller than the corresponding single-parameter fits for the same subsample (Table 1). For example, in the case of the full sample of 182 galaxies, the multiparameter fit in Table 2 has AIC ≈ 103.0 while the best single-parameter fit in Table 1 (using $\log(M_*/M_\odot)$) has AIC ≈ 112.7 , so including the extra parameters appears to do a better job of predicting the presence of P+Sh profiles. Since only the Hubble-type parameter in this multiparameter fit has a marginally significant ($P_{\beta=0} \approx 0.01$) slope in the multiparameter fit, it appears that the gas mass fraction $\log f_{\text{gas}}$ is not meaningful.

If we restrict ourselves to the B/P-detection subsample, then the possible significance of Hubble type as a secondary parameter disappears. If we also include the $g-r$ colour and bar strength $A_{2,\text{max}}$ (for the 125 galaxies in the full sample that have both values – see the final fit in the table), then $g-r$ is a marginally significant ($P_{\beta=0} \approx 0.035$) secondary parameter, while the Hubble type and $A_{2,\text{max}}$ are *not*.

In summary, it appears that galaxy mass (M_* or V_{rot}) is the only clear determinant for the presence of absence of P+Sh profiles,

although there is the possibility that $g-r$ colour could be a secondary parameter.

4.3 Exponential and related bar profiles

One of the key findings of this paper is that the classic ‘Exponential’ bar-profile type actually consists of several distinct sub-types. In addition to what we call exponential profiles (which have a single exponential slope from the centre to the end of the bar), we also identify Two-Slope and Flat-Top profiles (Section 3 and Figs 3–5).

Two-Slope bar profiles are a rarity, accounting for only $7.1^{+2.7}_{-2.0}$ per cent of the non-P+Sh bars. Flat-top bars are more significant, making up one quarter (25 ± 4 per cent) of the non-P+Sh bars. Figs 6 and 7 show no evidence for any differences in stellar mass, Hubble type, or gas fraction between Two-Slope, Flat-Top, and Exponential profiles; as noted in Section 4.1, K-S tests for these different sub-types show no evidence for statistically significant differences in their stellar-mass distributions. Further K-S tests for possible differences in terms of Hubble type, gas mass fraction, or bar strength yielded nothing significant, with the possible exception of a difference between Hubble types for 2S profiles and the other two subtypes, in the sense the 2S Hubble types are more evenly distributed and less concentrated towards very late Hubble types ($P \sim 0.02$). The significance of this is, however, borderline, especially considering that we are testing multiple comparisons (e.g. 2S versus non-2S for various different galaxy parameters).

5 THE LINK BETWEEN B/P BULGES AND BAR PROFILES

As noted in Section 1.2, recent research has suggested that ‘flat’ bar profiles are associated with bars that have B/P bulges, with the shoulder part of the profile corresponding to the outer, vertically thin part of the bar and the B/P bulge having a steeper surface brightness profile that produces most of the ‘peak’ of the P+Sh profiles.

This has two obvious implications. The first is that most if not all bars with B/P bulges should have P+Sh profiles. The second is the inverse: most if not all P+Sh profiles should be in bars with B/P bulges. In this section of the paper, we test these ideas by identifying which bars do and do not have B/P bulges from a morphological perspective. To do so, we use the B/P-detection subsample, where we can maximize our ability to detect both the presence and absence of B/P bulges inside the bars.

5.1 Determining the frequency of B/P bulges as a function of galaxy properties

Erwin & Debattista (2017) analysed near-IR images of a local sample of 84 barred galaxies which had orientations favorable for detecting B/P bulges. They found a very strong, almost perfectly monotonic dependence of B/P-bulge morphology on stellar mass: galaxies with masses $< 10^{10}$ almost never had B/P bulges, while galaxies with masses $> 10^{10.5}$ almost always had them. They found supporting evidence for this trend in the SDSS analysis of Yoshino & Yamauchi (2015). Subsequently, Li et al. (2017) used optical images from the Carnegie-Irvine Galaxy Survey (Ho et al. 2011) to argue for a very similar trend (e.g. their figure 3), using both the morphological signature identified by ED13 and the ‘barlens’ morphology identified by Laurikainen and collaborators (e.g. Laurikainen et al. 2011; Athanassoula et al. 2015; Laurikainen & Salo 2017), which is visible in more face-on galaxies. Kruk et al. (2019) found the same trend using SDSS images for $z \sim 0$ barred galaxies, and hints that the trend

might be present in higher-redshift galaxies. More recently, Marchuk et al. (2022) found a very similar result for B/P bulges identified in edge-on galaxies.

The original analysis of Erwin & Debattista (2017) had some disadvantages. In particular, it included a galaxy angular diameter limit ($D_{25} > 2'$), which translates to a bias against physically compact galaxies. Consequently, we decided to repeat the same morphological analysis using the B/P-detection subsample of our S4G-based sample, which is strictly distance-limited and includes 132 galaxies; since rotation velocity measurements are available for all of the galaxies, we also look for trends in B/P fraction as a function of V_{rot} . We note that Erwin & Debattista (2017) included some S0 galaxies in their sample, while here we are restricted to spiral galaxies only.

5.2 Identification of B/P bulges in bars

Erwin & Debattista (2013) showed that B/P bulges in bars could be identified via characteristic patterns in the bar isophotes, as long as the galaxy was moderately inclined (e.g. $i \sim 40\text{--}75^\circ$) and the bar was not too close to the galaxy minor axis (see also Erwin & Debattista 2016, 2017). This took the form of what they called a ‘box + spurs’ morphology, where the B/P bulge itself projected to form a thick, often boxlike structure (the ‘box/oval’) and the outer vertically thin part of the bar projected to form narrower isophotes (the ‘spurs’). As long as the bar was oriented more than a few degrees away from the galaxy’s major axis, these two structures were misaligned in a characteristic way, with the spurs rotated further away from the major axis than the box/oval. (See Fig. 1 for examples, as well as figures in the aforementioned papers.) An important corollary of this morphology was the fact that when a B/P bulge was *not* present, the bar showed symmetric elliptical isophotes *without* the box/oval + spurs morphology, meaning that it was possible to identify bars *lacking* B/P bulges as well.

5.3 Updated frequencies of B/P bulges

Fig. 9 shows how the fraction of bars with B/P bulges $f(B/P)$ behaves as a function of stellar mass in the B/P-detection subsample. The trend is a dramatic one: the B/P fraction is 0 per cent for $\log(M_*/M_\odot) < 9.5$ and 100 per cent for $\log(M_*/M_\odot) > 10.5$, with a monotonic and very steep transition between these two regimes. The thick dashed line shows the result of a logistic regression analysis. This indicates that $f(B/P) = 0.5$ at $\log(M_*/M_\odot) = 10.29$ and 0.9 at $\log(M_*/M_\odot) = 10.65$.

This trend is very similar to that seen for a smaller (and slightly overlapping) sample by Erwin & Debattista (2017), except that it is *stronger* for our newer, larger sample (we show the original logistic fit from Erwin & Debattista 2017 as thin dashed grey line, with $f(B/P) = 0.5$ at $\log(M_*/M_\odot) = 10.36$ and 0.9 at $\log(M_*/M_\odot) = 10.89$). We suspect this may be due to the more consistent stellar masses used in our current sample (all based on *Spitzer* 3.6 μm photometry); the more heterogeneous mass estimates in Erwin & Debattista (2017) could mean a greater scatter, and thus a weakening of the sharp transition.

There are 37 galaxies in the B/P-detection subsample which are also in the 84-galaxy ED17 sample, so some of the agreement *could*

¹⁵In Erwin & Debattista (2013), this was called the ‘box’, since in strong cases its isophotes were actually rectangular; however, in many cases the projected B/P bulge has oval isophotes, so we adopt the more general term box/oval in this paper.

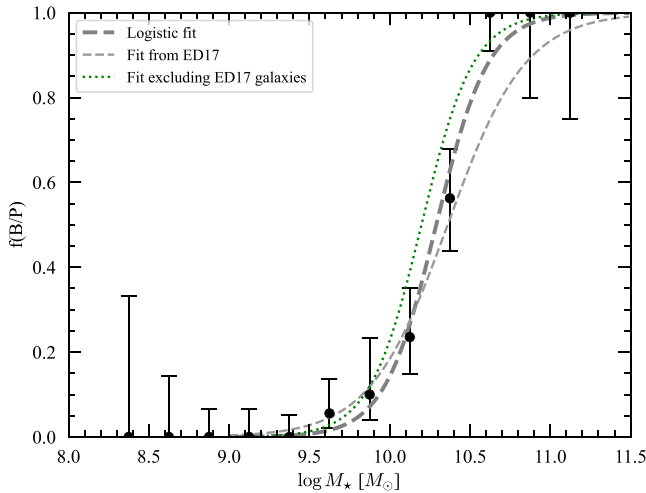


Figure 9. Frequency of B/P bulges within bars as a function of galaxy stellar mass, from our 132-galaxy B/P-detection subsample. The thick dashed curve shows the best-fitting logistic regression (fit to the full set of individual data points rather than the bins). The thin dashed curve is the logistic regression from Erwin & Debattista (2017), while the dotted (green) curve shows the logistic regression using the 95 galaxies in the B/P-detection subsample that are *not* in the original ED17 sample.

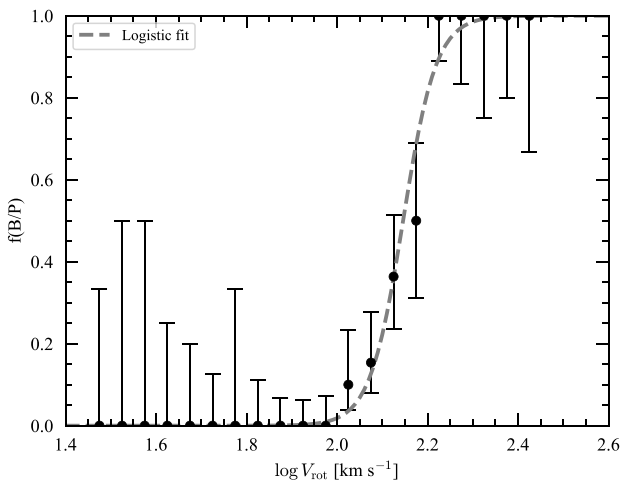


Figure 10. As for Fig. 9, but now showing the fraction of bars with B/P bulges as a function of galaxy rotation velocity.

be due to this overlap. We can eliminate this possibility by looking at the trend for just those 95 galaxies in the B/P-detection subsample which were *not* in the ED17 sample. This shows the same basic pattern; the logistic fit for this subsample is shown with the green line in Fig. 9. This increases our confidence in the general result, since essentially the same strong B/P-fraction–stellar-mass relation is found for two different galaxy samples.

Fig. 10 shows the trend in $f(B/P)$ as a function of galaxy (gas) rotation velocity, along with the corresponding logistic fit. The same strong trend is clearly visible. In this case, no galaxies with $V_{\text{rot}} < 100 \text{ km s}^{-1}$ have B/P bulges, while all galaxies with $\log V_{\text{rot}} > 2.2$ ($V_{\text{rot}} \sim 160 \text{ km s}^{-1}$) do. The existence of the Tully–Fisher relation means that this similarity is entirely to be expected, though it does raise the question of whether $f(B/P)$ might somehow depend on, e.g. halo mass rather than stellar mass. The AIC values for the logistic fits are 61.7 for the $\log(M_*/M_\odot)$ fit and 49.4 for the V_{rot} fit,

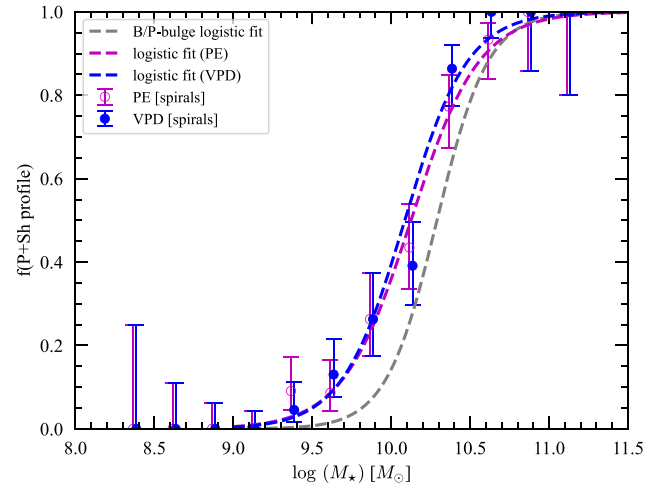


Figure 11. Frequency of P+Sh bar profiles in barred spiral galaxies (both subsamples combined) as a function of stellar mass; different symbols indicate results from the two classifiers. Dashed coloured curves show corresponding logistic fits. The grey dashed curve is the logistic fit for B/P-bulge presence from Fig. 9.

which indicates the latter is a better fit; the slope for the V_{rot} fit is clearly steeper (logistic slope = 27.0 ± 6.0 versus 6.1 ± 1.3 for the $\log(M_*/M_\odot)$ fit), indicating a stronger trend. Of course, residual uncertainties in the stellar-mass estimation might still introduce scatter into the latter relation, so we cannot really conclude that halo mass is the primary driver.

5.4 Peak+Shoulders profiles and the presence of B/P bulges

We now examine possible connections between B/P bulges and bar profiles. We first look at bars in the B/P-detection subsample with identified B/P bulges (as a reminder, this sample is made of galaxies with inclinations and bar orientations selected to maximize the ability to detect B/P bulges, if they are present). Essentially *all* such bars have P+Sh profiles: we securely classify 30 of the 32 B/P-bulge hosts as having P+Sh profiles – and for the two galaxies not unambiguously classified (NGC 4498 and NGC 7513), the classifications were split, with one of the two classifiers labeling them P+Sh.

What about the inverse? Do we find P+Sh profiles in galaxies whose bars *lack* B/P bulges? There are in fact nine galaxies in the B/P-detection subsample which both classifiers deemed to have P+Sh profiles, but for which we found little or no evidence for B/P bulges (the two classifiers differed on four other galaxies without B/P bulges, with one P+Sh and one non-P+Sh classification for each). Thus, it appears that P+Sh profiles *can* sometimes occur in the absence of B/P bulges.

The strong mass dependence seen for B/P bulges (Subsection 5.3) is replicated in the strong mass dependence of P+Sh profiles, as can be seen in Fig. 11. There is a clear implication: either one of these things *causes* the other (e.g. the buckling instability that gives rise to B/P bulges also produces P+Sh bar profiles), or both are linked to some common underlying mechanism. The fraction of bars with P+Sh profiles is slightly *higher* than the B/P-bulge fraction at all masses (that is, at all masses where the fractions are >0 and <1). The logistic fits suggest that the P+Sh fraction reaches 50 percent at $\log(M_*/M_\odot) \approx 10.1$, while the B/P-bulge fraction reaches 50 percent at $\log(M_*/M_\odot) \approx 10.3$ (compare the plotted

curves in Fig. 11). A K-S test gives $P = 0.0059$ for the null hypothesis that B/P hosts with P+Sh profiles and non-B/P hosts with P+Sh profiles come from the same parent distribution of stellar masses, so there is some suggestion of a real difference in the stellar-mass distributions.¹⁶ If bars form earlier and/or evolve faster in higher-mass galaxies, then this might be an indication that formation of the P+Sh profiles *precedes* formation of B/P bulges (see Section 6.3), which could perhaps explain why the mass distribution of B/P hosts and non-B/P hosts with P+Sh profiles differs slightly.

6 DISCUSSION

6.1 Comparison with previous studies

Our results are generally quite consistent with the original work by Elmegreen & Elmegreen (1985), Elmegreen et al. (1996), and Regan & Elmegreen (1997): we find a strong segregation of profile type with Hubble type, in the sense that P+Sh profiles (corresponding to the earlier ‘flat’ profile type) are preferentially found in earlier-type spirals and non-P+Sh profiles (corresponding to the earlier ‘exponential’ type) are preferentially found in late-type spirals. However, we argue on the basis of our multiparameter logistic fits (Section 4.2) that the Hubble-type dependence is basically a side effect of a more fundamental dependence on galaxy mass.

The studies of Kim et al. (2015) and Kruk et al. (2018) both suggested a strong dependence of bar-profile type – parametrized via the Sérsic index of the bar component in their 2D image decompositions – on stellar mass. Kim et al. (2015) argued for a transition between ‘flat’ (bar-component Sérsic $n < 0.4$) and ‘exponential’ ($n \geq 0.8$) occurring at $\log(M_*/M_\odot) \approx 10.2$. This is very similar to our transition mass of $\log(M_*/M_\odot) \approx 10.1$, defined as the point where the fraction of bars with P+Sh profiles reaches 50 per cent in our logistic regression (Section 5.4). Kruk et al. (2018) found a difference in Sérsic bar index between their low-mass bin ($\log(M_*/M_\odot) < 10.25$), where $n_{\text{bar}} = 0.81 \pm 0.60$, and their high-mass bin ($\log(M_*/M_\odot) \geq 10.25$), where $n_{\text{bar}} = 0.43 \pm 0.47$.

Both Kim et al. (2015) and Kruk et al. (2018) also pointed to associations between B/T values and bar-profile types. For example, Kim et al. argued, “The majority of exponential bars are in bulgeless galaxies, and all galaxies with $n_{\text{bar}} > 0.7$ are bulgeless galaxies. Thus, bar profiles can be better separated by bulge dominance and bulge types than by galaxy mass.” Similarly, Kruk et al. noted that low values of the bar Sérsic index (corresponding to flatter, outer, bar profiles) were strongly associated with ‘obvious bulge’ galaxies (i.e. those that required an extra Sérsic component for the ‘bulge’ in their image decompositions), while more exponential-like bar profiles were associated with ‘disc dominated’ galaxies.

Although we do not consider B/T values for our galaxies, the bulge–bar-profile associations of Kim et al. (2015) and Kruk et al. (2018) can be understood in the context of our findings if we recall that our P+Sh profile is the *combination* of a shallow-to-flat outer profile and a steep inner profile. Thus, a P+Sh bar is naturally best represented in a 2D fit by the combination of a low- n Sérsic component for the outer part of the bar and an additional, smaller and higher- n Sérsic component for the inner part of the profile. Our argument is that the steep inner part of the bar’s profile should *not* be seen as a separate (spheroidal) ‘bulge’, but rather as the

combination of the bar’s B/P structure and any additional inner non-bar components (nuclear discs, nuclear bars, actual spheroids, etc.) that may be present.¹⁷ Similar arguments have been made in the context of 2D image fitting of bars by Neumann et al. 2019 and Erwin et al. 2021.

Lee, Ann & Park (2019) suggested that flat-bar profiles are significantly more common in SB bars than in SAB bars. In our sample, we find no evidence for this – in fact, the opposite is true, though not at a statistically significant level. The fact that Lee et al. found over one-third of their *unbarred* galaxies to have flat profiles suggests their method of deriving profiles (combining amplitudes from Fourier analyses of deprojected images) may not produce the same results as ours.

Finally, we have argued that ‘Exponential’ bar profiles really fall into three subclasses: single-exponential (Exp), two-slope (2S), and flat-top (FT). This raises a question: why were 2S and FT profiles not identified in earlier studies? A perusal of Elmegreen & Elmegreen (1985), Elmegreen et al. (1996), and Regan & Elmegreen (1997) shows only 10 definite exponential profiles. Since the profiles from Elmegreen & Elmegreen (1985) were from centrally saturated images, making it difficult or impossible to identify central deviations from a single-exponential profile, we concentrate on the seven exponential-profile galaxies from Elmegreen et al. (1996) and Regan & Elmegreen (1997).¹⁸ Two of these were classified as part of our sample; we performed similar classifications for the other five galaxies (NGC 925, NGC 1359, NGC 1744, NGC 2835, and NGC 7741).

Of these seven ‘classical exponential’ profiles from the literature, we find one to be ambiguous (P+Sh according to one classifier, Exponential according to the other), with the remaining six are Exponential profiles. Since 68 per cent of the non-P+Sh bars in our sample are Exponential rather than 2S or FT, it is plausible that previous studies have missed the presence of FT and 2S bar profiles due to small-number statistics.

6.2 Comparison with theory

As noted in the Introduction (Section 1.1), theoretical work attempting to explain the origin of bar profiles has been relatively scant. In this section, we address some of what has been done in this area.

Athanassoula & Misiriotis (2002) noted differences in bar profiles in three different N -body simulations. The clearest case of a P+Sh profile – indeed, probably the first instance of a simulation producing a proper P+Sh profile – was in their ‘massive halo’ model, while the ‘massive disc’ model had a bar with an approximately exponential profile. Unfortunately, since we have no kinematic information for the vast majority of our galaxies, we cannot test whether the observed profiles might correlate with different halo-density profiles or different relative halo–disc concentrations.

Anderson et al. (2022) analysed an ensemble of barred-galaxy simulations (mostly N -body, but including three with gas and star formation) using an algorithm for detecting and measuring the presence of shoulders in the surface-density profiles of bar major axes. They also checked for bar buckling and the presence or absence of B/P bulges (this included cases where B/P bulges formed gradually *without* strong buckling).

¹⁶The median stellar mass of the non-B/P P+Sh galaxies is $\log(M_*/M_\odot) \sim 10.2$, while for the P+Sh galaxies with B/P bulges it is ~ 10.6 .

¹⁷We remind the reader that there is some evidence for a small subset of bars with P+Sh profiles but no B/P bulge (Section 5.4).

¹⁸*Spitzer* IRAC1 images indicate that NGC 3184 is not actually barred (e.g. Buta et al. 2015; Herrera-Endoqui et al. 2015), so we exclude this galaxy.

They identified numerous instances of shoulders – what we would term P+Sh profiles – and found that the shoulders were primarily made up of particles trapped around looped x_1 orbits. The formation of shoulders appeared to be tied to the secular evolution of the bar, and in particular of the *growth* of the bar, so that shoulders did not appear when the bar did not grow.

Since the focus of Anderson et al. (2022) was on P+Sh profiles, the different instances of *not*-P+Sh profiles were not classified. Their Figs 7 and 8 show that such profiles tended to be pure exponential. However, in a few cases the profile showed a Flat-Top shape, usually very early on (i.e. immediately after bar formation), and then evolved into an Exponential profile (and often then on to P+Sh).

They noted that B/P bulges and P+Sh profiles were commonly but not always associated in their simulations, including cases where B/P bulges formed *before* shoulders and cases where secondary buckling eliminated shoulders, transforming (or returning) the profile to exponential. This is in partial disagreement with our observational findings: while we do find some bars with P+Sh profiles that do not have B/P bulges, we find no instances of the opposite. One possible implication might be that secondary buckling, which should result in B/P bulges without P+Sh profiles, is quite rare in real galaxies.

6.3 Timing considerations

In Section 5.4, we noted that while all bars with B/P bulges show P+Sh profiles, there are some bars with P+Sh profiles that do not seem to have B/P bulges. This suggests a possible scenario where P+Sh profiles form first, before the appearance of B/P bulges. In this section, we make some crude duty-cycle estimates to see if we can relate the observed frequencies to possible time-scales – in particular, we sketch out an estimate of what fraction of the time bars might spend with P+Sh profiles before forming B/P bulges.

For simplicity, we assume that bars form (or re-form) at some uniform rate in time R , and that they have a finite lifetime L ; the number of barred galaxies is then $N_{\text{bar}} = RL$. (If bars have lifetimes longer than the current age of the Universe, then L is the time since bars started forming.) We also assume that there is a delay time T_1 between bar formation and the formation of the P+Sh profile, and a further delay time T_2 between P+Sh profile formation and the formation of an observable B/P bulge. Thus, the number of barred galaxies with P+Sh profiles is $N_{\text{P+Sh}} = R(L - T_1)$ and the number of barred galaxies with both P+Sh profiles and B/P bulges is $N_{\text{both}} = R(L - T_1 - T_2)$, so the number of barred galaxies with P+Sh profiles but *without* B/P bulges is just $N_{\text{P+Sh-only}} = RT_2$. This lets us see that the ratio of galaxies with P+Sh but no B/P bulges to all barred galaxies is $N_{\text{P+Sh-only}}/N_{\text{bar}} = T_2/L$.

For our sample, $N_{\text{P+Sh-only}}/N_{\text{bar}} \approx 0.068$, which implies that the typical time between P+Sh formation and B/P formation is ~ 0.07 of the bar lifetime. If bars are permanent (or at least have lifetimes longer than the current age of the universe) and began forming ~ 10 Gyr ago (e.g. Guo et al. 2023), then the time between P+Sh formation and B/P formation would be ~ 0.7 Gyr.

7 SUMMARY

We have presented an analysis of volume- and mass-limited samples of barred spiral galaxies (excluding lenticulars) wherein we revisit the classic question, first raised by Elmegreen & Elmegreen (1985), of what forms the major-axis surface-brightness profiles of bars can take. We argue that the classic dichotomy first reported by Elmegreen & Elmegreen (1985) – that bar profiles fall into ‘flat’

and ‘exponential’ types – is better understood in terms of *four* profile types:

(i) Peak+Shoulders (P+Sh): This is an update of the traditional flat-bar profile. In such bars, the inner part of the profile forms a steep central *peak* (in combination with additional, non-bar structures such as classical bulges, nuclear discs, secondary bars, etc.), while the outer part of the profile forms a *shoulder*: a shallower (sometimes actually flat) subsection with an outer break to a steeper falloff.

(ii) Exponential: This a bar-major-axis profile that is essentially a pure exponential extending into the centre of the galaxy (ignoring local variations due to star formation and nuclear star clusters).

(iii) Two-Slope (2S): This is a profile with a shallow inner exponential and a steeper outer exponential.

(iv) Flat-Top (FT): Here, the inner part of the bar profile is approximately flat (i.e. constant surface brightness), with a steeper falloff in the outer part of the bar.

The three non-P+Sh profile types (Exponential, 2S, and FT, with Exponential being the most common) are effectively subsets of the original exponential type of Elmegreen & Elmegreen (1985). Our subdivision of this type comes from the fact that we consider the entire bar-major-axis profile, extending into the centre of the galaxy, rather than just the outer part of the bar as in most previous studies; this enables us to see differences in the inner parts of bars that have otherwise similar outer profiles.

We find a very strong mass segregation for the different profile types, in the sense that P+Sh bars are found in high-mass galaxies, while the other types are found in low-mass galaxies (with no clear difference between their distributions). This is consistent with the original study of Elmegreen & Elmegreen (1985), which found flat profiles in early-type spirals and exponential profiles in late-type spirals, when one takes into account the fact that late-type spirals are generally lower in mass than early-type spirals, and thus more prone to host bars in the ‘exponential sub-family’ (Exponential, Two-slope, or Flat-Top).

P+Sh and non-P+Sh bars are also segregated by (neutral) gas fraction, global galaxy colour, and (weakly) bar strength, with P+Sh bars preferentially found in gas-poor and redder galaxies, and those with stronger bars. A careful analysis shows, however, that these trends (as well as the Hubble-type trend) are mostly if not entirely *side effects* of the dominant mass-segregation trend: there is no clear evidence for any dependence of bar-profile type on Hubble type or gas fraction, once the dependence on mass is controlled for, and only weak evidence for a possible additional dependence on colour. Additionally, we find no evidence for a systematic difference in (relative) bar size or strength between P+Sh and non-P+Sh bars once stellar mass is accounted for.

As part of our analysis, we classify a subsample of bars in an inclination- and bar-position-angle-limited subsample (B/P-detection subsample) into those with and without B/P bulges inside their bars. In line with previous work (Erwin & Debattista 2017; Li et al. 2017; Marchuk et al. 2022), we find a very strong dependence of B/P presence on galaxy stellar mass (or, equivalently, gas rotation velocity V_{rot}); this dependence is even stronger than found for the smaller sample of Erwin & Debattista (2017), possibly because we use a more consistent set of stellar mass estimates in this paper.

We find a near-perfect match between bars with B/P bulges and the P+Sh class: when a bar has an identifiable B/P bulge, its major-axis profile is P+Sh, with the peak being due to the steep profile of the B/P bulge (plus any extra, non-bar components near the centre) and the shoulders associated with the vertically thin outer part of the bar. There is a small population of bars lacking B/P bulges

which nevertheless have P+Sh profiles, mostly at intermediate stellar masses ($\log(M_*/M_\odot) \sim 10.2$); this may be a hint that formation of P+Sh profiles *precedes* the formation of B/P bulges.

ACKNOWLEDGEMENTS

We would like to thank the referee, Bruce Elmegreen, for useful comments and questions, as well as Lia Athanassoula, Leandro Beraldo e Silva, Adriana de Lorenzo-Cáceres, Martin Herrera-Endoqui, Johan Knapen, Zhao-Yu Li, and Jerry Sellwood for various helpful comments and suggestions. We also thank the anonymous author of *Sir Gawain and the Green Knight* for certain bits of inspiration.

This work is based in part on observations made with the *Spitzer* Space Telescope, obtained from the NASA/IPAC Infrared Science Archive, both of which are operated by the Jet Propulsion Laboratory, California Institute of Technology under a contract with the National Aeronautics and Space Administration. This paper also makes use of data obtained from the Isaac Newton Group Archive which is maintained as part of the CASU Astronomical Data Centre at the Institute of Astronomy, Cambridge.

The Legacy Surveys consist of three individual and complementary projects: the Dark Energy Camera Legacy Survey (DECaLS; Proposal ID #2014B-0404; PIs: David Schlegel and Arjun Dey), the Beijing-Arizona Sky Survey (BASS; NOAO Prop. ID #2015A-0801; PIs: Zhou Xu and Xiaohui Fan), and the Mayall z-band Legacy Survey (MzLS; Prop. ID #2016A-0453; PI: Arjun Dey). DECaLS, BASS, and MzLS together include data obtained, respectively, at the Blanco telescope, Cerro Tololo Inter-American Observatory, NSF's NOIRLab; the Bok telescope, Steward Observatory, University of Arizona; and the Mayall telescope, Kitt Peak National Observatory, NOIRLab. The Legacy Surveys project is honoured to be permitted to conduct astronomical research on Iolkam Du'ag (Kitt Peak), a mountain with particular significance to the Tohono O'odham Nation.

NOIRLab is operated by the Association of Universities for Research in Astronomy (AURA) under a cooperative agreement with the National Science Foundation.

This project used data obtained with the Dark Energy Camera (DECam), which was constructed by the Dark Energy Survey (DES) collaboration. Funding for the DES Projects has been provided by the U.S. Department of Energy, the U.S. National Science Foundation, the Ministry of Science and Education of Spain, the Science and Technology Facilities Council of the United Kingdom, the Higher Education Funding Council for England, the National Center for Supercomputing Applications at the University of Illinois at Urbana-Champaign, the Kavli Institute of Cosmological Physics at the University of Chicago, Center for Cosmology and Astro-Particle Physics at the Ohio State University, the Mitchell Institute for Fundamental Physics and Astronomy at Texas A&M University, Financiadora de Estudos e Projetos, Fundação Carlos Chagas Filho de Amparo, Financiadora de Estudos e Projetos, Fundação Carlos Chagas Filho de Amparo à Pesquisa do Estado do Rio de Janeiro, Conselho Nacional de Desenvolvimento Científico e Tecnológico and the Ministério da Ciência, Tecnologia e Inovações, the Deutsche Forschungsgemeinschaft, and the Collaborating Institutions in the DES. The Collaborating Institutions are Argonne National Laboratory, the University of California at Santa Cruz, the University of Cambridge, Centro de Investigaciones Energéticas, Medioambientales y Tecnológicas-Madrid, the University of Chicago, University College London, the DES-Brazil Consortium, the University of Edinburgh, the Eidgenössische Technische Hochschule Zürich,

Fermi National Accelerator Laboratory, the University of Illinois at Urbana-Champaign, the Institut de Ciències de l'Espai (IEEC/CSIC), the Institut de Física d'Altes Energies, Lawrence Berkeley National Laboratory, the Ludwig Maximilians Universität München and the associated Excellence Cluster Universe, the University of Michigan, NSF's NOIRLab, the University of Nottingham, the Ohio State University, the University of Pennsylvania, the University of Portsmouth, SLAC National Accelerator Laboratory, Stanford University, the University of Sussex, and Texas A&M University.

BASS is a key project of the Telescope Access Programme, which has been funded by the National Astronomical Observatories of China, the Chinese Academy of Sciences (the Strategic Priority Research Programme 'The Emergence of Cosmological Structures' Grant # XDB09000000), and the Special Fund for Astronomy from the Ministry of Finance. The BASS is also supported by the External Cooperation Programme of Chinese Academy of Sciences (Grant # 114A11KYSB20160057), and Chinese National Natural Science Foundation (Grant # 11433005).

The Legacy Survey team makes use of data products from the Near-Earth Object Wide-field Infrared Survey Explorer (NEOWISE), which is a project of the Jet Propulsion Laboratory/California Institute of Technology. NEOWISE is funded by the National Aeronautics and Space Administration.

The Legacy Surveys imaging of the DESI footprint is supported by the Director, Office of Science, Office of High Energy Physics of the U.S. Department of Energy under contract no. DE-AC02-05CH1123, by the National Energy Research Scientific Computing Center, a DOE Office of Science User Facility under the same contract; and by the U.S. National Science Foundation, Division of Astronomical Sciences under contract no. AST-0950945 to NOAO.

The Siena Galaxy Atlas was made possible by funding support from the U.S. Department of Energy, Office of Science, Office of High Energy Physics under Award Number DE-SC0020086 and from the National Science Foundation under grant AST-1616414.

This research also made use of Astropy, a community-developed core PYTHON package for Astronomy (Astropy Collaboration 2022).

DATA AVAILABILITY

The data underlying this article, along with code for reproducing fits and figures, are available at <https://doi.org/10.5281/zenodo.7545179>. (*Spitzer* images for all galaxies can be found at, e.g. the NASA Extragalactic data base: <https://ned.ipac.caltech.edu>.)

REFERENCES

- Anderson S. R., Debattista V. P., Erwin P., Liddicott D. J., Deg N., Beraldo e Silva L., 2022, *MNRAS*, 513, 1642
- Astropy Collaboration, 2022, *ApJ*, 935, 167
- Athanassoula E., 2005, *MNRAS*, 358, 1477
- Athanassoula E., Beaton R. L., 2006, *MNRAS*, 370, 1499
- Athanassoula E., Misiriotis A., 2002, *MNRAS*, 330, 35
- Athanassoula E., Laurikainen E., Salo H., Bosma A., 2015, *MNRAS*, 454, 3843
- Beraldo e Silva L., Debattista V. P., Anderson S. R., Valluri M., Erwin P., Daniel K. J., Deg N., 2023, *ApJ*, in press
- Blañá Díaz M., Wegg C., Gerhard O., Erwin P., Portail M., Opitsch M., Saglia R., Bender R., 2017, *MNRAS*, 466, 4279
- Bureau M., Freeman K. C., 1999, *AJ*, 118, 126
- Buta R., Laurikainen E., Salo H., Block D. L., Knapen J. H., 2006, *AJ*, 132, 1859
- Buta R. J. et al., 2015, *ApJS*, 217, 32
- Combes F., Elmegreen B. G., 1993, *A&A*, 271, 391

Combes F., Debbasch F., Friedli D., Pfenniger D., 1990, *A&A*, 233, 82
 Díaz-García S., Salo H., Laurikainen E., Herrera-Endoqui M., 2016, *A&A*, 587, A160
 Elmegreen B. G., Elmegreen D. M., 1985, *ApJ*, 288, 438
 Elmegreen B. G., Elmegreen D. M., Chromey F. R., Hasselbacher D. A., Bissell B. A., 1996, *AJ*, 111, 2233
 Erwin P., 2018, *MNRAS*, 474, 5372
 Erwin P., 2019, *MNRAS*, 489, 3553
 Erwin P., Debattista V. P., 2013, *MNRAS*, 431, 3060
 Erwin P., Debattista V. P., 2016, *ApJ*, 825, L30
 Erwin P., Debattista V. P., 2017, *MNRAS*, 468, 2058
 Erwin P. et al., 2021, *MNRAS*, 502, 2446
 Gadotti D. A., Athanassoula E., Carrasco L., Bosma A., de Souza R. E., Recillas E., 2007, *MNRAS*, 381, 943
 Georgiev I. Y., Böker T., 2014, *MNRAS*, 441, 3570
 Guo Y. et al., 2023, *ApJ*, 945, L10
 Herrera-Endoqui M., Díaz-García S., Laurikainen E., Salo H., 2015, *A&A*, 582, A86
 Herrera-Endoqui M., Salo H., Laurikainen E., Knapen J. H., 2017, *A&A*, 599, A43
 Ho L. C., Li Z.-Y., Barth A. J., Seigar M. S., Peng C. Y., 2011, *ApJS*, 197, 21
 Kim T. et al., 2015, *ApJ*, 799, 99
 Kruk S. J. et al., 2018, *MNRAS*, 473, 4731
 Kruk S. J., Erwin P., Debattista V. P., Lintott C., 2019, *MNRAS*, 490, 4721
 Kuijken K., Merrifield M. R., 1995, *ApJ*, 443, L13
 Laurikainen E., Salo H., 2017, *A&A*, 598, A10
 Laurikainen E., Salo H., Buta R., Knapen J. H., 2011, *MNRAS*, 418, 1452
 Laurikainen E., Salo H., Athanassoula E., Bosma A., Herrera-Endoqui M., 2014, *MNRAS*, 444, L80
 Lee Y. H., Ann H. B., Park M.-G., 2019, *ApJ*, 872, 97
 Li Z.-Y., Ho L. C., Barth A. J., 2017, *ApJ*, 845, 87
 Marchuk A. A. et al., 2022, *MNRAS*, 512, 1371
 Meidt S. E. et al., 2012, *ApJ*, 744, 17

Méndez-Abreu J., Corsini E. M., Debattista V. P., De Rijcke S., Aguerri J. A. L., Pizzella A., 2008, *ApJL*, 679, L73
 Muñoz-Mateos J. C. et al., 2015, *ApJS*, 219, 3
 Neumann J. et al., 2019, *A&A*, 627, A26
 Noguchi M., 1996, *ApJ*, 469, 605
 Querejeta M. et al., 2015, *ApJS*, 219, 5
 Raha N., Sellwood J. A., James R. A., Kahn F. D., 1991, *Nature*, 352, 411
 Regan M. W., Elmegreen D. M., 1997, *AJ*, 114, 965
 Salo H. et al., 2015, *ApJS*, 219, 4
 Seigar M. S., James P. A., 1998, *MNRAS*, 299, 672
 Sheth K. et al., 2008, *ApJ*, 675, 1141
 Sheth K. et al., 2010, *PASP*, 122, 1397
 Springob C. M., Haynes M. P., Giovanelli R., Kent B. R., 2005, *ApJS*, 160, 149
 Wegg C., Gerhard O., Portail M., 2015, *MNRAS*, 450, 4050
 Yoshino A., Yamauchi C., 2015, *MNRAS*, 446, 3749

APPENDIX A: BAR-PROFILE PLOTS USED FOR BLIND CLASSIFICATIONS

Fig. A1 shows examples of the actual profile plots used for our classification. To evaluate the possible exponential nature of the profiles, we plotted an automatic exponential fit to the profile from the centre to the bar radius (dashed lines in Fig. A1). In the top two panels, the bar profiles match quite well with the exponential fits, and we would classify both profiles as Exponential. The bottom two plots show strong P+Sh profiles, with the outer parts of the shoulders protruding above the exponential fit, the inner shoulder and the outer part of the peak lying clearly below the fit, and the central peak standing well above the extrapolation of the fit to $r = 0$.

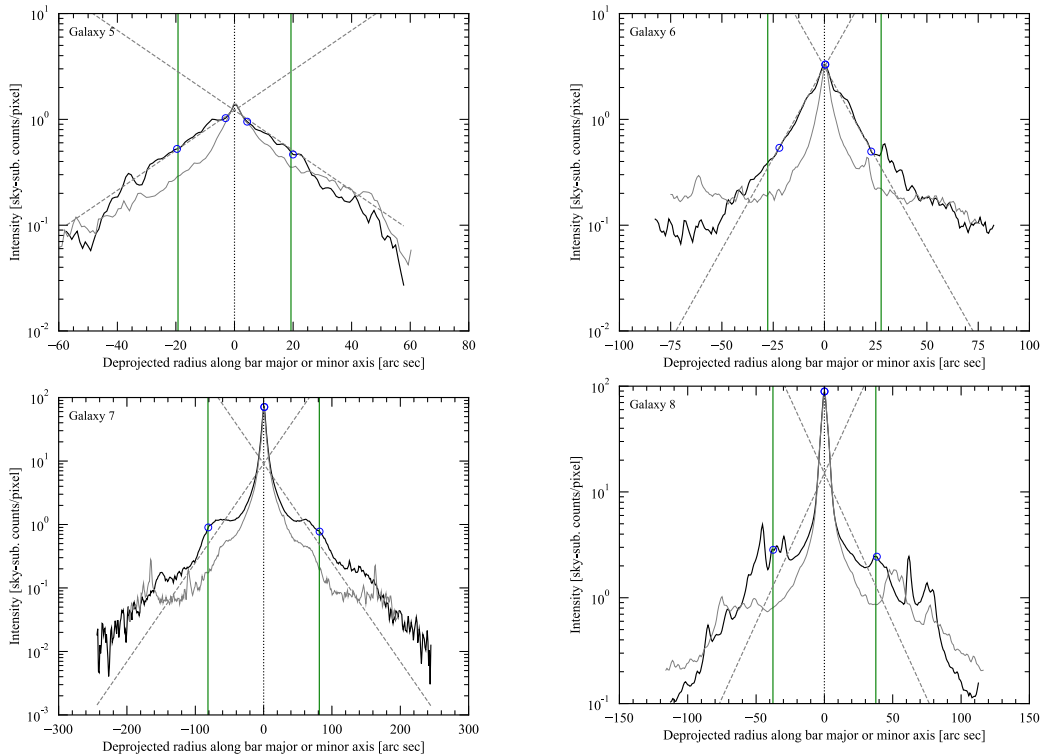


Figure A1. Examples of the profile plot format used for our blind classifications. Solid lines indicate the bar-major-axis profile while thin grey lines show the bar-minor-axis profile. Vertical green lines mark the bar radius. Dashed diagonal lines show simple exponential fits to the bar-major-axis profiles, using data between the open circles.

This paper has been typeset from a \LaTeX file prepared by the author.

© 2023 The Author(s)

Published by Oxford University Press on behalf of Royal Astronomical Society